DIATOMIC EXCIMER DYNAMICS IN MICROPLASMA LAMPS AND ALKALI LASERS

BY

SEHYUN PARK

DISSERTATION

Submitted in partial fulfillment of the requirements
for the degree of Doctor of Philosophy in Electrical and Computer Engineering
in the Graduate College of the
University of Illinois at Urbana-Champaign, 2019

Urbana, Illinois

Doctoral Committee:

Professor J. Gary Eden, Chair
Professor Brian T. Cunningham
Professor Xiuling Li
Associate Professor Virginia Lorenz
Associate Professor Davide Curreli

ABSTRACT

The dynamics of diatomic excimers - electronically excited molecules having dissociative ground states - generated in alkali-rare gas mixtures and low temperature microplasmas have been pursued and the experimental and computational results are presented here. This work focuses on the Cs-rare gas and He_2 molecules that are of considerable interest as efficient near-infrared lasers, or as the energy source for driving the Hg^+ vacuum-ultraviolet lamp (194.2 nm). The photoassociation and subsequent stimulated emission of cesium (Cs) - rare gas (Ar or Xe) pairs were examined by laser pump-probe experiments, and an optical-to-optical energy conversion efficiency of $\sim$28% was observed when Cs-Ar pairs were pumped at 836.7 nm and stimulated emission occurs at 852.2 nm. By comparing full quantum simulations of Cs-Xe photoassociation to the gain spectrum of Cs-Xe in the red satellite of the Cs D_2 line, it is shown that the structure of weakly bound Cs-Xe molecules (including the dissociation energy), correlated with $Cs(6^2P_{3/2})$ + $Xe(5p^6\ ^1S_0)$ in the separated atom limit, can be determined with precision. Extensive studies of time-resolved emission from the Hg^+ ion in electrically driven microplasma lamps show that the Hg^+ line at 194.2 nm is pumped efficiently by Penning ionization of the Hg atom by metastable helium molecules. Experimental results as well as zero-dimensional kinetic simulations support the validity of the proposed kinetic pathway.

To my parents, for their love and support.

ACKNOWLEDGMENTS

One of the most important things that I realized during my doctoral program is that I would not be able to go this far without help and support from others. I am very grateful and feel indebted to many people who helped me start and finish the doctoral study at the University of Illinois.

First of all, I am a beneficiary of the culture and experience of the Laboratory of Optical Physics and Engineering (LOPE). I was fortunate enough to have all the great colleagues and study in the incredible environment created by the former and current members of the laboratory. I would like to thank my friend, mentor, and advisor, Professor J. Gary Eden. His insight on research and support led me in the right direction. He taught me not only a way to live a life as a researcher, but also how I should spend the dinner time to be a better man. Gary was much more than just an advisor. Thank you, Gary, for everything. Professor Sung-Jin Park helped me to learn the fabrication techniques and practical knowledge related to microplasmas. As a chief technology officer in Eden Park Illumination, his experience has been very helpful in fabricating microplasma lamps. Dr. Andrey Mironov is my predecessor in alkali laser research and guided me to a better direction whenever I was lost. He has been generous in sharing his knowledge and experience with me. If Gary was my father in LOPE, Andrey was like my older brother. I learned many fabrication skills from Dr. Hee Jun Yang and Dr. Chul Shin and they have been great lunchmates. We have been through many experiences together and I really enjoyed the time with you two. Jinhong Kim helped me to deposit coating materials on the microplasma lamp and he was a good friend to talk with. It was always amusing to talk with Rui, Austin, and Kavita about academic subjects and all the creative jokes.

There are also many staff members to whom I would like to thank in the Electrical and Computer Engineering Department in University of Illinois. Christi was always trying to help whenever I had trouble solving adminis-

tration issues. When I was struggling for the first couple of years, she was always supportive. Bev was not hesitant to help me solve many issues. Clint was always greeting me with his smile. Jan helped me edit both my M.S. and Ph.D theses. I would not be able to have these two fine theses without her help.

I was also able to get technological and practical advice from fellows in EPI. Dr. Cy Herring guided me with his vast knowledge. Ted, Stephen, and David have always been supportive on whatever I asked in lamp fabrication. Kathy was always kind to help me process administration related to the mercury lamp.

I received a scholarship from Jeongsong Cultural Foundation covering the tuition and the living expense for the first two years. Without the opportunity that Jeongsong offered, I was not even able to begin the Ph.D program in Illinois. I am very grateful for the financial support.

I have many family members and friends that I appreciate. My grandmother and grandfather raised me and always trusted me. Their love and wisdom are irreplaceable. Father, you are a good father much more than you think. My uncle is a wise man and supported me mentally and financially. I appreciate my aunt for her careful concern. Jenna, I am a fortunate man to be with you. Thank you for being the best friend and partner.

TABLE OF CONTENTS

CHAPTER 1

INTRODUCTION

Excimer

The interaction potential for two ground state rare gas atoms is largely dissociative aside from a van der Waals minimum. The van der Waals force is so weak that the attraction by the force is negligible compared to kT at room temperature. For example, the van der Waals minimum of xenon dimer is 107 cm^{-1} while kT in 298 K is 207 cm^{-1} [1]. This implies that the two atoms can be regarded as a colliding pair. However, if one of the pairs is in the excited state, they are able to form a metastable dimer. This dimer is known as an "excited dimer" or an "excimer". A similar term "exciplex" is an abbreviation of "excited complex" and it often refers to a case that two atoms are different elements while one of the atoms is a rare gas. However, in this work, excimer will be used as a comprehensive term that includes both cases. Potential curves for the ground state of the rare gas dimer and helium excimers can be found in [2], [3].

Due to its bound-free molecular transition, diatomic excimers have distinct features when compared to other gaseous media that utilize bound-bound transition for radiation. Excimer has been mainly utilized as an excimer laser since 1970 [4]. Since the ground state of the excimer is repulsive, the lower molecular state can be depopulated quickly after the radiative transition, which makes a population inversion easily achievable. Also, it has been shown that lasing occurs in the UV/VUV region in halogen-rare gas mixtures with a peak power exceeding 100 MW. Since the technology utilizes a gaseous medium, the beam quality and thermal stability are ensured. These distinctive features of halogen-rare gas excimer lasers such as ArF (193 nm) and KrF (248 nm) have made enormous progress in the semiconductor industry by accessing small feature sizes down to 10 nm in material processing.

XPAL

A different type of gas laser, DPAL (Diode-pumped alkali laser), has been introduced a decade ago [5]. The laser system has a gain medium that consists of alkali vapor, such as Rb or Cs, and a buffer gas [6], [7], [8]. The D_2 line ($n^2P_{3/2} \rightarrow n^2S_{1/2}$) is optically pumped and lasing occurs at D_1 line ($n^2P_{1/2} \rightarrow n^2S_{1/2}$). The buffer gases are often hydrocarbon (methane or ethane) and rare gases. They induce a spin-orbit mixing so that non-radiative relaxation from $n^2P_{3/2}$ to $n^2P_{1/2}$ is more efficient compared to the pure alkali vapor system, but they are the main reason for unwanted chemical reactions responsible for the degradation of the window of the gas cell. While embracing all the advantages of the gaseous medium, the alkali laser has shown a considerable quantum efficiency. For example, the quantum efficiency is larger than 98% in the case of cesium. The extraordinary quantum efficiency is attributed to the small energy defect between $n^2P_{3/2}$ and $n^2P_{1/2}$ of alkali atom. Furthermore, it has been shown that lasing power can reach 1.5 kW and the optical-to-optical efficiency is demonstrated to be $\sim$56% [9], [10], [11] in continuous wave (CW) operation pumped by a laser diode. However, in order to obtain such high efficiencies and lasing power, the linewidth of the laser diode has to be narrowed to match the linewidth of D_2 of the alkali atom. Otherwise, only a portion of the pumping power is absorbed to the gain medium due to the mismatch between the broad linewidth of the diode laser and the narrow linewidth of the absorption line which is the D_2 line. A volume Bragg grating (VBG) is often used to narrow the linewidth of the output from the commercial laser diodes.

Several years after the invention of DPAL, a new concept called XPAL (Exciplex-pumped alkali laser) has been proposed by Readle *et al.* [12]. The lasing medium consists of alkali vapor and rare gas. The blue satellite of the D_2 line of alkali metal appears when rare gas is introduced in the system because of the atomic interaction of the alkali atom and rare gas atom. Since it is a free-free molecular transition, the linewidths of the blue satellites are often greater than 5 nm. This feature allows the system to be used with commercial diode lasers without any complicated line-narrowing techniques. In addition, undesirable chemical reactions with hydrocarbons in XPAL can be avoided because collisional quenching between the atomic resonance states is not required.

Excimer Lamp

Although excimers have been primarily exploited as gain media in lasers, they can also be used as a high power UV/VUV spontaneous emission source. Various types of the gas mixture that have been commercialized as excimer lamps [13]. As in excimer lasers, excimer lamps also show high efficiency and intense radiation in the UV/VUV region. For instance, Park *et al.* [14] have recently shown xenon excimer lamps having a peak power of 850 W with an electrical-to-optical conversion efficiency larger than 20%. The UV/VUV lamp emitting 7.2 eV photons with such high intensity has not been accessible in the past. The technology has high potentials in material processing and environmental applications. Among various types of plasma discharges to produce excimer emission, the microplasma system is promising since it produces excimers efficiently due to its operation in high pressure up to the atmospheric pressure and the high electron temperature (1-5 eV). Furthermore, miniaturization of the lamp can be realized and volumetric emission can be enhanced significantly using microplasmas. For example, a microplasma lamp can be designed as a flat tile to produce spatially uniform VUV emission as demonstrated in [14].

Aims of the Work

In this work, two different applications that utilize the traits of excimers will be suggested. First, the alkali-rare gas mixture will be investigated in a pump-and-probe experimental arrangement. Efficiency of the gain medium in nanosecond optical pulses will be determined. Furthermore, an unprecedented type of an optical amplifier that relies on free-free molecular transition on both of pumping and amplifying process will be proposed.

The other application is a microplasma mercury lamp designed to drive a mercury ion atomic clock. The upper state of the desired transition is located $\sim$16 eV above from the ground state of the mercury. The state is difficult to reach by the electron impact processes in the typical low-temperature plasma system which has an average electron temperature of only a few eV. In the current work, however, helium excimer will be utilized as a collisional pair for ionization and excitation to populate the upper state of the 194.2 nm transition. Helium excimer has a long lifetime and is easily formed in the microplasma system. In the way that helium excimers collide with mercury atoms, the upper state of a mercury ion is readily accessible. Experimental

result will show that helium is the most efficient to produce 194.2 nm radiation compared to other rare gases such as neon and argon. Temperature and pressure dependence of the UV/VUV spectrum is a clue that excimer collision acts an important role to produce intense 194.2 nm radiation. In order to fully grasp the kinetic pathway of the process, zero-dimensional kinetic simulation will be performed.

CHAPTER 2

THEORETICAL BACKGROUND

2.1 Franck-Condon Principle

Franck-Condon Principle

Initiated from the consideration of the spectrum produced during photodissociation of diatomic molecules by Franck [15], Condon [16] further developed the idea to interpret the relative intensities of the vibrational structure in the spectrum attributed to bound-bound molecular transition. The transition is represented by a vertical line in the potential curve, which implies that the position and momentum of the nuclei is conserved during the electronic transition. Thus, the Franck-Condon principle assumes that the motion of the nuclei is sluggish during electronic transition, which also can be found in Born-Oppenheimer approximation. The dipole transition moment can be written as a product of two integral overlaps [17],

$$\boldsymbol{\mu} = \int_0^\infty \psi'(-e \cdot \mathbf{r})\psi'' dR \propto \int_0^\infty \psi'_v \psi''_v dR \int_0^\infty \psi'_e(-e \cdot \mathbf{r})\psi''_e dR \qquad (2.1)$$

where $\boldsymbol{\mu}$ is the dipole transition moment, ψ is the total wavefunction, ψ_v is the vibrational wavefunction, ψ_e is the electronic wavefunction, $(-e \cdot \mathbf{r})$ is the electric dipole moment. The former integral on the right side is the Franck-Condon overlap integral which is the overlap integral of the vibrational wavefunctions of the upper and the lower states. The latter integral is the electric-dipole transition moment, $\boldsymbol{\mu_e}$. $\boldsymbol{\mu_e}$ is a function of R, but the R-dependence is often neglected (Condon approximation), which makes it constant in the Franck-Condon calculation.

The square of the Franck-Condon overlap integral is called the Franck-

Condon factor and it is proportional to the line strength, S_{AB},

$$S_{AB} \propto \left| \int_0^\infty \psi'_v \psi''_v dR \right|^2 = |< \psi'_v \mid \psi''_v >|^2 \tag{2.2}$$

The absorption and emission coefficient is proportional to S_{AB}. For example, the absorption coefficient [18],

$$\sigma_{v,ab}(v'', J'') \propto \nu \, |< \psi'(v'_J) \mid \psi''(v''_J) >|^2 \tag{2.3}$$

For the bound-free transition, diffuse spectra are observed because one of the wavefunctions are continuum. In this case, the discrete wavefunctions are replaced by the vibrational continuum which represents the free molecular states,

$$\sigma_{v,ab}(v'', J'') \propto \nu \, |< \psi'(\epsilon'_J) \mid \psi''(v''_J) >|^2 \tag{2.4}$$

Quasi-static Line Broadening

The qausi-static line broadening [18], [19] is a classical method to describe the Franck-Condon density in terms of the probability distribution, $P(R)$.

$$|< \psi'(\epsilon'_J) \mid \psi''(v''_J) >|^2 \approx P(R_\nu) \left| \frac{dV(R)}{dR} \right|^{-1}_{R_\nu} \tag{2.5}$$

where V is the difference potential. The absorption coefficient is larger as the denominator is closer to zero. The zero denominator means the upper and lower potentials are parallel to each other. The method is often used to determine the line shape or satellite structures of atomic resonance lines [20].

2.2 Microplasma

Microplasma as an Excimer Source

Plasmsas confined in small dimensions less than a milimeter are difined as microplasmas [21]. Microplasmas show distinctive characteristics compared

to bulk plasma states. Stable glow discharges are possible in high pressure up to the atmospheric pressure. The Paschen law [22] which determines the breakdown voltage of gases as a function of a scaling factor called pd(Torr·cm)

$$V_B = \frac{Bpd}{\ln(Apd) - \ln(\ln(1 + \frac{1}{\gamma_{se}}))} \tag{2.6}$$

where V_B(V) is the breakdown voltage, p(Torr) is the pressure of the gas, d(cm) is the distance between the cathode and the anode, γ_{se}(unitless) is the secondary-electron-emission coefficient, A(cm^{-1}·Torr^{-1}) and B(V·cm^{-1}·Torr^{-1}) are obtained experimentally for different gases.

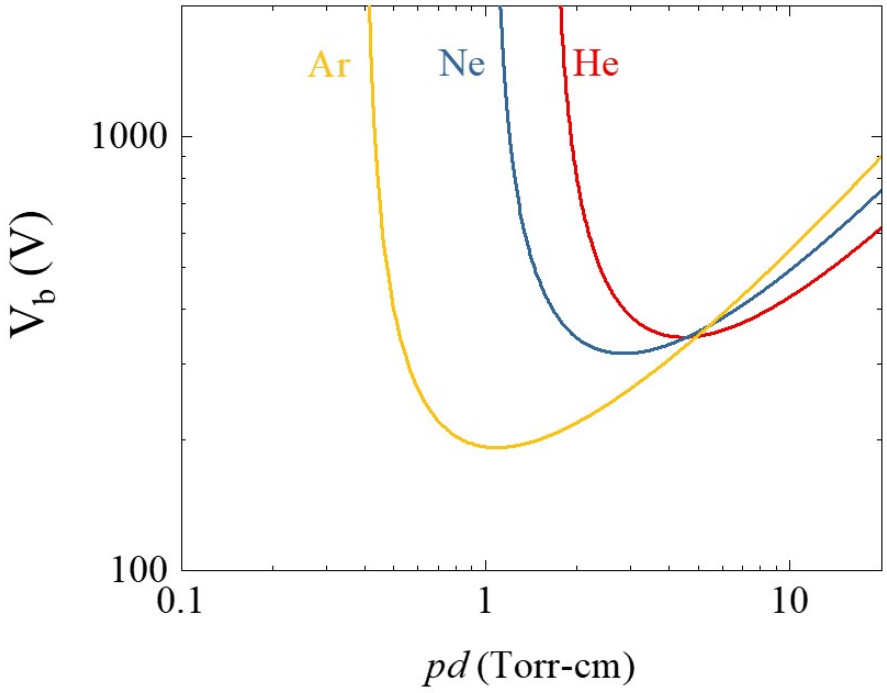

Figure 2.1: Paschen curves plotted for noble gases with the coefficients given in [22].

When the discharge voltage is given, the pd value determines the mean free path of a free electron between the collisions with the background neutral atoms when it is accelerated by the external electric field created between the cathode and the anode. The Paschen curve is shown in Figure 2.1 for several rare gases [22]. While they show different minimum values of the breakdown voltages for different rare gases, the shape is similar since it is

governed by Equation 2.6. As the value of pd decreases or increases from the value for the minimum breakdown voltage, the breakdown voltage increases. As the pd increases, the free electrons cannot gain enough kinetic energy for ionizing the neutral gases between collisions. On the other hand, if the pd is too small, the free electrons do not experience a large enough number of collisions for cascade ionization before it reaches to the anode.

Although the microplasma do not follow strictly to the Paschen curve in small scale less than 10 μm for many reasons such as field emission and strong surface-plasma interaction [23], the pd scaling gives a clue on why microplasmas are able to operate in high pressure. The electrode distance d in microplasmas is small, thus p is higher to the obtain the minimum breakdown voltage. For example, in the case of He, the pd is $\sim$5 Torr·cm for the minimum breakdown voltage in Figure 2.1. In the atmospheric pressure (760 Torr), the d is $\sim$65 μm. Thus, the microplasmas are allowed to operate as stable glow discharge modes in the atmospheric pressure.

Furthermore, the high electron density can be obtained in microplasmas with the short voltage pulse by electron heating effect [24]. The electron energy distribution function (EEDF) is known to shift to the higher energy resulting in the non-Maxwellian distribution with pulsed operation with a pulse duration less than the glow-to-arc transition. The higher average electron temperature results in the higher electron density. The electron densities up to $\sim 10^{16}$ cm^{-3}-10^{17} cm^{-3} have been reported in microcavity discharges in Ar [25], [26].

The two features discussed above, the high pressure operation and high electron density, make the microplasma the efficient source for the generation of rare gas excimers. In general, two steps are required to form an excimer in plasmas. First, the ground state atoms have to be excited to the high electronic state. Then, dimerization of the excited atom with another neutral atom produces an excimer molecule. The energies required to excite the ground state atoms to the first excited state are 8.3-19.8 eV from Xe to He. Thus, the free electrons with the kinetic energies above these values are able to contribute to excite the ground state atoms to the high electronic states by direct impact excitation. The highly non-Maxwellian electron energy distributions of pulsed microplasmas enable the efficient excitation of the gases. Dimerization of an excited atom with a neutral atom is much more efficient in the presence of another neutral atom for conservation of the mo-

mentum [27]. The three-body character of the process makes the conversion rate proportional to the square of the gas pressure, making it more preferable in higher pressure.

The efficient generation of excimers in microplasmas has been reported with various types of experimental schemes and operating conditions. Frame *et al.* [28] demonstrated the excimer emission on the I_2, XeI, and XeO in the microchannels fabricated on silicon driven by a DC voltage source. Excimer emission on the Ar_2^* in MHCDs with a hole diameter of 130 μm in a pulsed operation showed the peak power of 180 mW with at efficiency of 5-6% [25]. Recently, a VUV excimer emission on Xe_2 in a large array of microcavity plasmas has shown the efficient generation of 172 nm with the average power more than 25 W [14].

Of particular interest is the report of the He_2 excimer emission in a microcavity discharges by Kurunzi *et al.* [29]. They demonstrated not only the possibility of the generation of the He_2 excimer emission in $\sim$75 nm in microplasmas but also the fact that the He_2 molecular metastables collide with the impurity gases to produce the highly excited states of the impurities which require the energy ranging between 12.40-20.38 eV in total.

Therefore, microplasmas are efficient sources for the generation of an excimer molecule which could be both a radiative or metastable species. The metastable excimer can be utilized as a collision partner for energy transfer to other species allowing the selective population of the highly excited states.

CHAPTER 3

EXCIPLEX-PUMPED ALKALI LASER

In this chapter, two types of optically pumped alkali lasers will be investigated in a pump-and-probe experimental arrangement. The mixture of cesium vapor and rare gases is utilized for the study. In Section 3.1, the characteristics of the gaseous medium will be introduced. Amplification of 852.1 nm in Cs-Ar will be studied in Section 3.2. In Section 3.3, a Cs-Xe optical amplifier based on free-free molecular transition both on absorption and amplification will be discussed. In Section 3.4, the Franck-Condon calculation of the red satellite of the Cs-Xe medium will be shown and compared to the experimental result.

3.1 Cs-Rg Gaseous Medium

Interatomic potential curves of the $B^2\Sigma^+_{1/2}$ and the $X^2\Sigma^+_{1/2}$ states for Cs-Ar (blue) and Cs-Xe (green) are shown in Figure 3.1 [30]. The potential curves are responsible for the shape of the absorption and emission spectrum of the medium. The atomic resonance transition of the D_2 line of cesium is indicated as a purple arrow at the infinite internuclear separation showing that the radiation wavelength is 852.1 nm in air. The van der Waals minima for the $X^2\Sigma^+_{1/2}$ states of Cs-Ar and Cs-Xe are 42.9 cm^{-1} and 105.8 cm^{-1}, respectively. The bump at around 5 Å in the $B^2\Sigma^+_{1/2}$ state is caused by perturbation mainly by 5^2D states [31]. This feature enables the existence of the blue satellite absorption band. Two red lines on the left side of the graph indicate the interatomic spacing responsible for the blue satellites of Cs-Ar and Cs-Xe.

Figure 3.2 shows the absorption spectrum of the cesium cells with two different buffer gases, Ar and Xe, while the rare gas number density is 2.8×10^{19} cm^{-3} corresponding to 800 Torr in pressure. The results are obtained from an

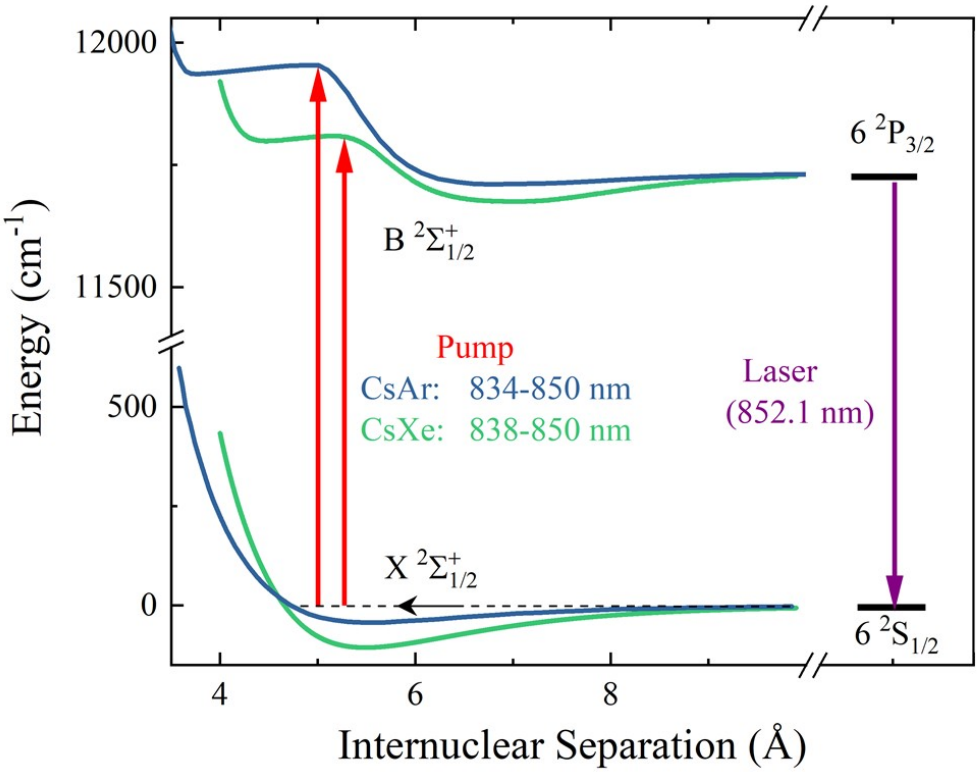

Figure 3.1: Interatomic potential curves for Cs-Ar and Cs-Xe.

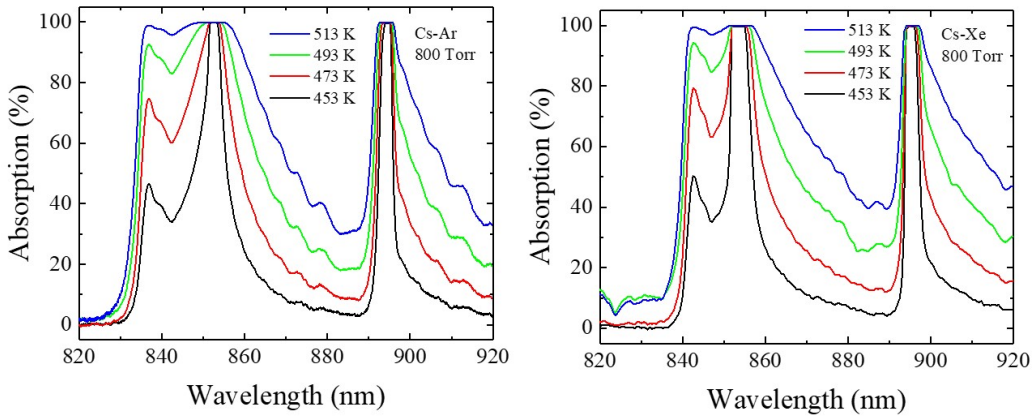

Figure 3.2: Absorption spectrum of Cs-Ar 800 Torr and Cs-Xe 800 Torr at different temperatures.

optical spectrum analyzer (AQ6317B, Ando) and a laser-driven white light source (EQ-99X, Energetiq). The white light is collimated and passes the

cell in the axial direction in an oven which controls the temperature. The beam, then, is focused to an optical fiber attached to the spectrum analyzer. The blue satellite is located on the blue side of the D_2 line where the peak wavelengths are 836.7 nm and 842.7 nm for Ar and Xe, respectively. The broad linewidths of the satellite bands are attributed to free-free molecular transition as shown in Figure 3.1. The linewidth is 5-10 nm in FWHM. The large value of the linewidth has drawn attention because it can be utilized in high-power alkali lasers pumped by the commercialized diode lasers [12]. The typical linewidth of the commercialized diode lasers is approximately 4 nm which matches to the linewidth of the blue satellite of the D_2 line in the alkali-rare gas mixture. With the general advantages of gaseous medium such as high beam quality, narrow linewidth, and thermal stability, the technique that utilizes the blue satellite as a pumping state is promising in high-power laser system.

A red wing and bound-free absorption structure are also seen on the red side of the D_1 and D_2 lines. The periodic structure on the red wing of the D_1 and D_2 lines is attributed to the bound-free transition of the $A^2\Pi_{1/2}$ and $A^2\Pi_{3/2}$ to the $X^2\Sigma^+_{1/2}$ state, respectively. The overall absorption increases as the temperature rises because the number density of cesium increases. The estimated number of cesium is labeled as an inset in Figure 3.2. The corresponding temperature is ranged between 453 K-513 K with a spacing of 20 K.

3.2 XPAL MOPA

The experimental arrangement and the optical beam path are presented in Figure 3.3. The pump and probe beams are generated from a double-dye laser system pumped by a double-frequency Nd:YAG laser. The duration of the pulses is 8 ns. The dye solution used in the experiment is LDS 821 dissolved in Dimethylsulfoxide (DMSO). The wavelengths of the beams are measured by a wavemeter (871, Bristol Instrument) with a precision of 0.0002 nm ($\sim$80 MHz). The energy stabilizer comprised of a half-wave plate and a polarizing beam splitter (PBS) is controlled by a feedback signal from Detectors 1 and 2. The optical delay ($\Delta t = t_{pump}$-t_{probe}) is 1 ns. The delay is experimentally measured by a photodiode probing an alkali-rare gas cell placed in an oven.

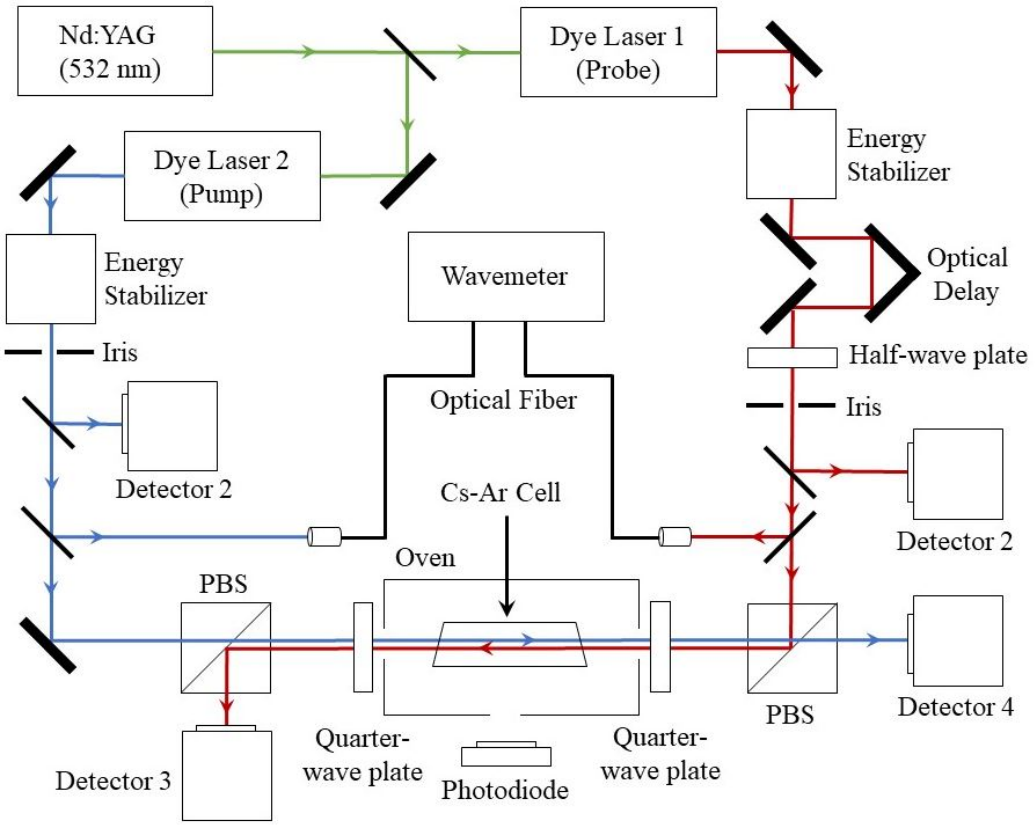

Figure 3.3: Experimental arrangement.

The probe beam from Dye laser 1 passes a half-wave plate so that the beam is vertically polarized while the pump beam is horizontally polarized. The beam size is limited by an opening of irises that have a diameter of 4 mm. Two quarter-wave plates are placed on both sides of the oven for circular polarization. The probe and pump energy after passing the alkali-rare gas cell are separated by a PBS and are detected by Detector 3 and Detector 4, respectively. The PIB controllers measure and control the temperature of the oven. The error range of the temperature is ± 3 K. The alkali-rare gas cell has a diameter of 25.4 mm and a length of 100 mm. Both windows are tilted by 11° to prevent parasitic oscillation.

The spectrum taken with the experimental setup described above is shown in Figure 3.4. A circularly or linearly polarized light is used to obtain the gain spectrum. The amplified spontaneous emission (ASE) is shown at the bottom to explain the non-zero baseline of the gain spectrum. The ASE is taken when the pump beam is present while the probe beam is blocked. The gap between the ASE and the baseline of the spectrum is matched to the value

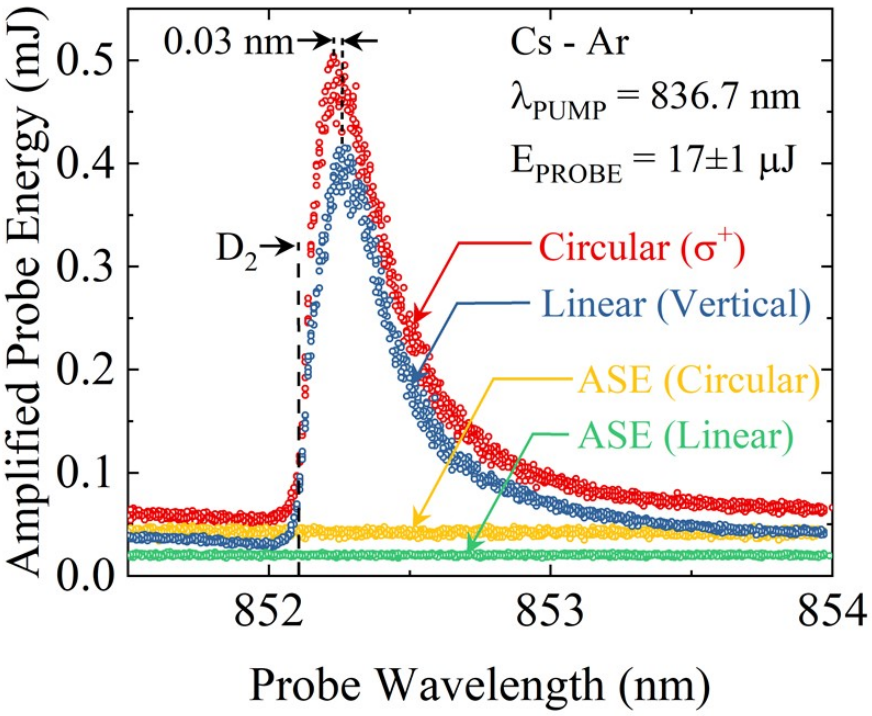

Figure 3.4: Amplified probe energy versus probe wavelength for Cs-Ar and Cs-Xe. Two different polarizations, linear and circular, are used for probe beam. The experimental conditions are described in the figure.

of the probe energy. The gas temperature is 483 K and the corresponding cesium number density is 2.6×10^{15} cm^{-3}. The pressure of argon buffer gas is 800 Torr and the corresponding gas number density is 2.8×10^{19} cm^{-3}. The pump energy and the wavelength are 4.3 mJ and 836.7 nm, respectively. The probe energy is fixed at 17 μJ while the probe wavelength is scanned throughout 851 nm to 854 nm.

The gain spectrum of the amplified probe energy near the D_2 line of cesium has a broad linewidth and an asymmetric form. The red wing is more significant compared to the blue side. This can be thought as the result of the shape of the interatomic potential curve since the pressure broadening is on the order of 0.01 nm while the resonance broadening is negligible due to the low number density of cesium [32], [33].

The potential curve is shown in Figure 3.5. On the right side where the internuclear separation goes to infinity, the atomic resonance states are shown. The absorption at the blue satellite is described by the up-arrow near the

internuclear separation at around 5 Å. In this process, the Cs and Ar are photoassociated into the transient exciplex molecule in the $B^2\Sigma^2_{1/2}$ state. However, since the potential is repulsive, the two atoms are not bound to each other. The two down-arrows near the resonance transition and the shaded region represent where the amplification occurs. The D_2 line is indicated by the dashed line in the gain spectrum in Figure 3.4. The peak of the gain spectrum is red-shifted to the D_2 line of Cs. Thus, it implies that the amplifying transition occurs at the free-molecular state, not as an isolated atomic resonance.

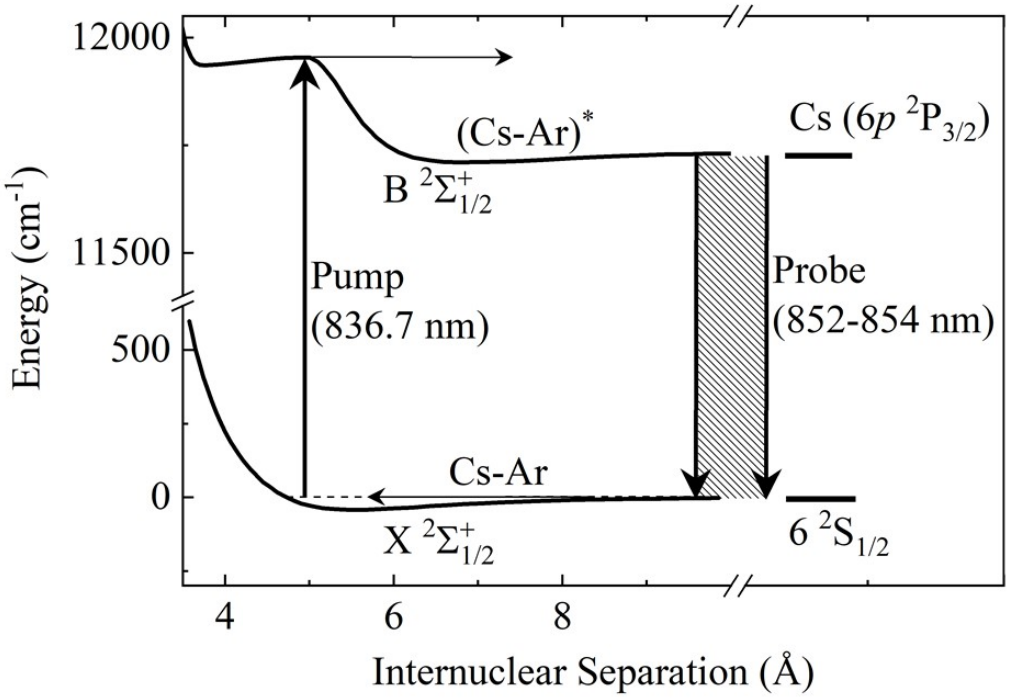

Figure 3.5: Interatomic potential curve for a Cs-Ar atomic pair.

Furthermore, the polarization of the pump and probe beams change the gain of the amplification. The circularly polarized pump beam selectively populates the $6^2P_{3/2}$ states of cesium which makes the population inversion effectively greater compared to the linear polarization case [34]. It should be also noted that the quarter wave-plates have not been placed for the linear polarization experiment. Thus, the circularly polarized beam shows a better amplifying efficiency in spite of the loss of the beam energy through the two quarter-wave plates. The peak value of the gain is also shifted to the blue

side by 0.03 nm. This results from the increased gain in competition with the self-absorption.

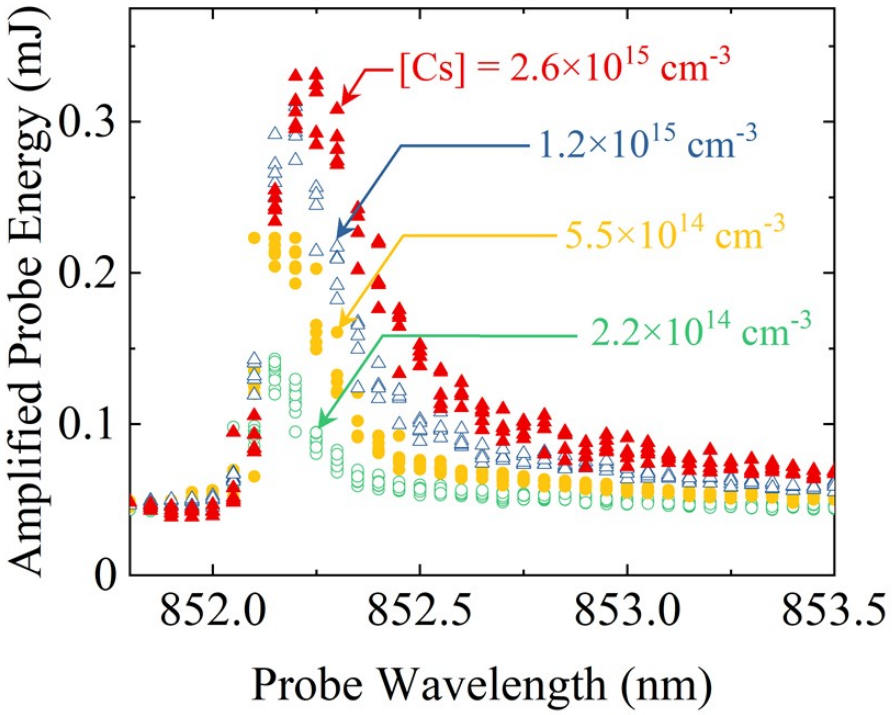

Figure 3.6: The gain spectrum of the Cs-Ar gas mixture for different cesium number density which is controlled by the temperature of the cell. The experimental conditions are described in the figure.

The cesium gas number density is changed as the temperature of the gas cell changes. The collision frequency of the cesium and rare gases correspondingly increases as the cesium number density increases. Figure 3.6 shows the dependence on the temperature of two gas cells on the gain spectrum. The gain and the shape of the spectrum changes as the cesium number density changes. While it shows the red shift of the gain peak and broadening of the gain, the peak value increases as the cesium number density increases until certain temperature. Although for argon cell did not show roll-over in the given temperature range, a cell filled with xenon showed a roll-over at a cesium number density around 5.2×10^{15} cm^{-3} which is shown later in Section 3.3. This is explained by the 4-2 energy level collapse that occurs when the energy defect of the laser system is comparable to the thermal energy of the gases ($E \approx kT$) [30]. The population inversion is achieved by the non-

radiative transition from the large vibrational energy to the low vibrational energy of the $B^2\Sigma^2_{1/2}$ state. If $E \approx kT$, thermal equilibrium of the gas system does not allow the molecule to possess the lower kinetic energy efficiently. The population between the vibrational states rather becomes comparable to each other, which makes the population inversion of the lasing transition less significant.

The shift and broadening of the gain peak is caused by the shorter mean distance between the cesium and the rare gas. The anisotropic shape of the broadening is also an indication that the line is broadened by the potential curve difference. From the interatomic potential curve, the weight of transition responsible for the shorter interatomic distance is larger when the mean distance of the pair decreases. Therefore, the gain spectrum can be manipulated by the temperature of the gas cell.

Figure 3.7 shows the efficiency of the amplifier versus pump energy at 483 K. The black dot represents the efficiency versus the absorbed pump energy while the red one is the same data points for the total pump energy. The pump energy is absorbed less when the pump energy is higher due to the depletion of the ground state. For example, the absorption of the pump beam is approximately 60% when the pump energy is 1 mJ while it is 40% when the pump energy is 4 mJ. The wavelength the pump beam is set to be the peaks of the blue satellite which are 836.7 nm. The wavelength and the energy of the probe beam is 852.2 nm and 17 μJ, respectively. The absorbed energy efficiency reaches 28% when the pump energy is 5 mJ. The incident energy efficiency rapidly rises after the threshold with increasing pump energy until 2 mJ and it asymptotically approaches to 11%.

Figure 3.8 is an excitation spectrum of cesium argon cell. In order to obtain the spectrum, the wavelength of the pump beam is scanned while the probe wavelength is set to be 852.2 nm which is the peak of the gain spectrum. The pump energy is constant throughout the wavelength as 2.9 mJ. The structure of the excitation spectrum is a result of the shape of the interatomic potential curve. Compared to the absorption spectrum in Figure 3.2, the blue wing is not observed while the structure of the blue satellite is still maintained. The difference in the absorption spectrum and emission spectrum gives a clue on which transition is responsible for certain structures in spectrum. The excitation spectrum may represent the spectral feature responsible for repulsive potential. Since the wavelength of the probe pulse is 852.2 nm which

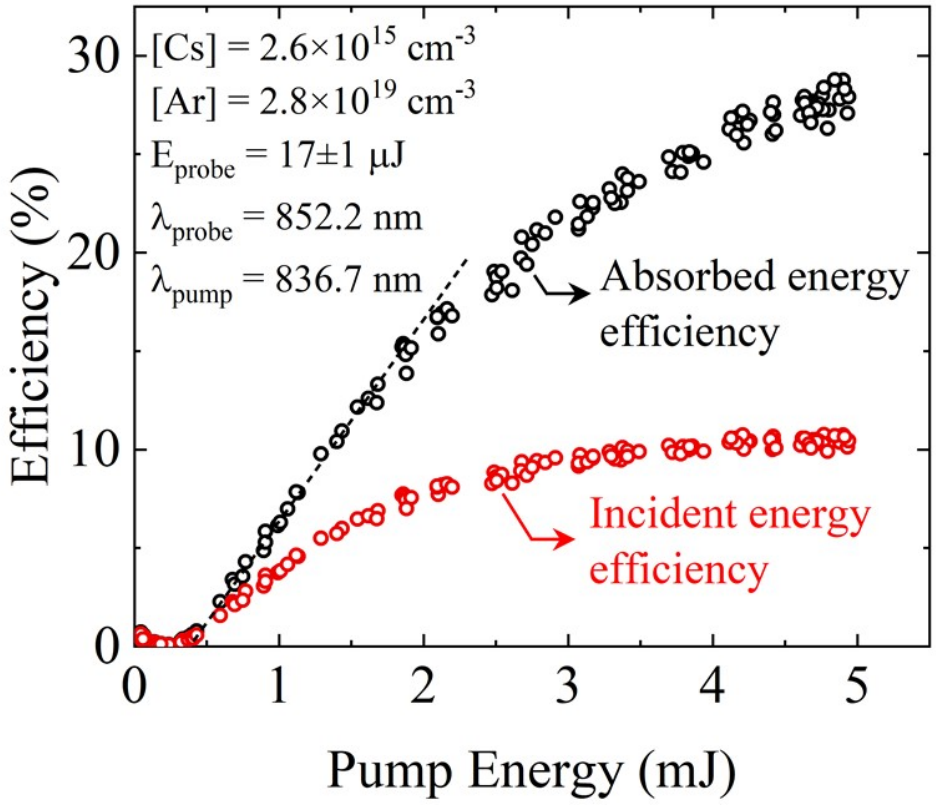

Figure 3.7: The efficiency curve for Cs-Ar gas mixture. The efficiency is defined as the output probe energy versus input pump energy. The black dot shows the efficiency versus absorbed pump energy while the red dot shows the same data points versus the total pump energy. The absorbed energy efficiency is approximately 28% which is corresponding to 11% as the incident energy efficiency when pump energy is 5 mJ.

is similar to the wavelength of the D_2 transition, 852.1 nm, the amplification occurs at the large interatomic distance. If the transient molecule is quenched into the vibrational or electronic states lower than the $6^2P_{3/2}$, the molecule cannot contribute to the excitation spectrum anymore. Thus, the excitation spectrum represents purely the repulsive character of the potential curve. Thus, the $B^2\Sigma^+_{1/2}$-$X^2\Sigma^+_{1/2}$ transition is responsible for the structure of the blue satellite. The long-range wing structure that extends from the D_2 transition is thought as the result of the $A^2\Pi_{3/2}$-$X^2\Sigma^+_{1/2}$ transition.

Different time delays between the pump and the probe pulse show the lifetime of the amplifying transition. After the molecules excited to the

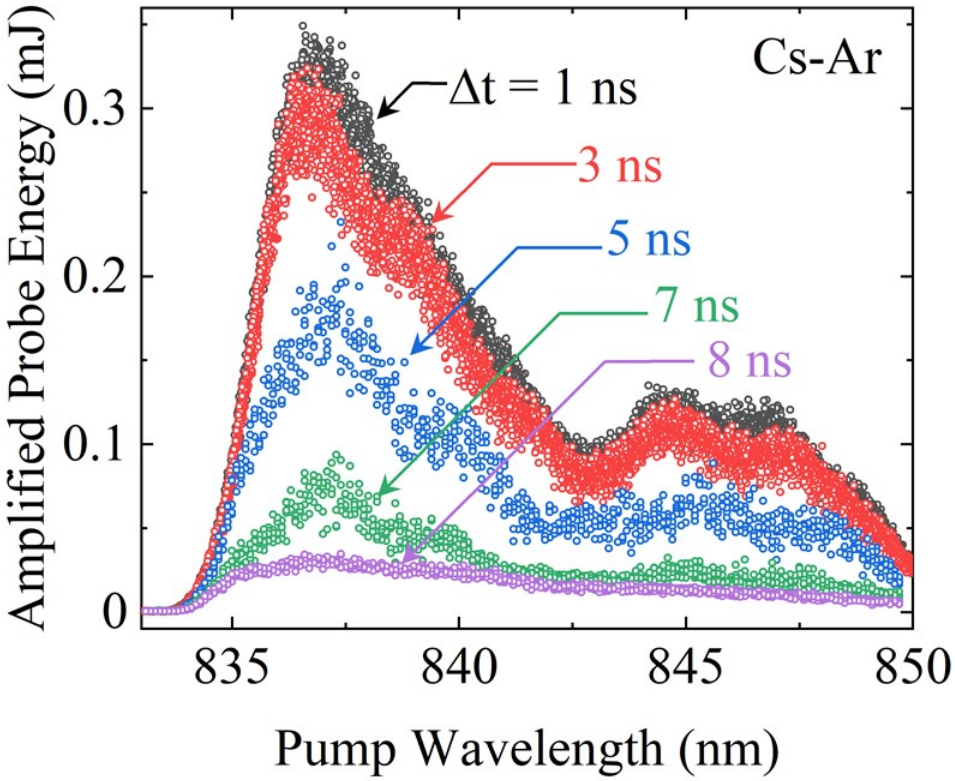

Figure 3.8: The excitation spectrum of the Cs-Ar gas mixture for the different time delay between the pump and probe pulse. The spectrum is obtained by scanning pump wavelength while the wavelength of the probe pulse is set to 852.2 nm.

$B^2\Sigma^+_{1/2}$ by the pump pulse, they experience the kinetic energy relaxation to thermal equilibrium. The excitation spectrum does not change much until the time delay of 2 ns, but it showed a reduction in the overall intensity and changes in the spectral features at 5 ns of the time delay which is shown as blue circles in Figure 3.8. The time constant of the decay of the peak value of the blue satellite is approximately 6 ns. This decay time can be regarded as the lifetime of the transient molecular state which is responsible for the amplifying transition. From the fact that the radiative lifetime of the $6^2P_{3/2}$ is $\approx$ 30 ns, the collisional lifetime of the transient molecule in 800 Torr is thought to be roughly 6 ns. It should be noted that the temporal overlap of the probe and pump pulse and the resultant dynamic needs to be included for more precise analysis.

The change in spectral features is also observed between the different time

delays. The kinetic energy relaxation changes the thermal distribution of the transient molecule and it changes the shape excitation spectrum as a result. The change is observed in the wavelength range between 838 nm and 842 nm in Figure 3.8. For the time delay of 1-3 ns, the bumped feature at 838 nm is somewhat similar to the absorption spectrum in Figure 3.2. However, for 5-7 ns of the time delay, the bump is moved to 840 nm.

The structure at 842-847 nm in Figure 3.2 may be attributed to three-body photoassociation (i.e., the photoexcitation of Ar-Cs-Ar trios). In the low pressure, this feature is not clearly shown. The interatomic potential curve can change its shape in the presence of another Ar atom near the Cs-Ar pair. The spectral feature appears as a result of the change in the potential curve.

3.3 Optical Amplifier Based on Free-Free Transition

Light emission or amplification in molecular states typically occurs in strong bound states because the lifetime of the species is large enough for the emission process to occur. The examples include homonuclear dimers such as N_2, O_2, Hg_2, and I_2 as well as heteronuclear dimers CO, HgBr, and ArF [18]. Large dissociation energy guarantees the long lifetime of the species. Once radiative transition occurs vertically in the potential curve, two atoms are repulsing each other, which results in fast elimination of the lower state subsequentially. This implies that population inversion is easily achieved in the system. Gas mixtures such as ArF or KrF laser is being utilized in semiconductor processing due to due to high efficiency as well as the lasing wavelength in vaccum ultra-violet (VUV). A decade ago, Readle *et al.* [12] reported that alkali-rare gas can absorb light in free-free molecular transition in high pressure operation up to the atmospheric pressure and lase at the D_1 line of cesium. However, light amplification in free-free transition has not been reported yet. In this section, an optical amplification in the red satellite of the D_2 line of cesium will be discussed. The amplification is possibly attributed to free-free molecular transition. A gas mixture of cesium and xenon is optically pumped through the free-free molecular transition and emits light also through free-free molecular transition.

The experimental arrangement is the same as the Cs-Ar MOPA experiment

in Section 3.2 except the gas cell used. In the work, a gas mixture of Cs vapor and Xe buffer gas was used while the pressure of Xe buffer gas varies between 800-1200 Torr. The pump beam is absorbed by the blue satellite of the D_2 line and the amplification occurs in the red satellite of the D_2 line. The wavelengths of the blue and red satellite are 842.7 nm and 854.5 nm, respectively.

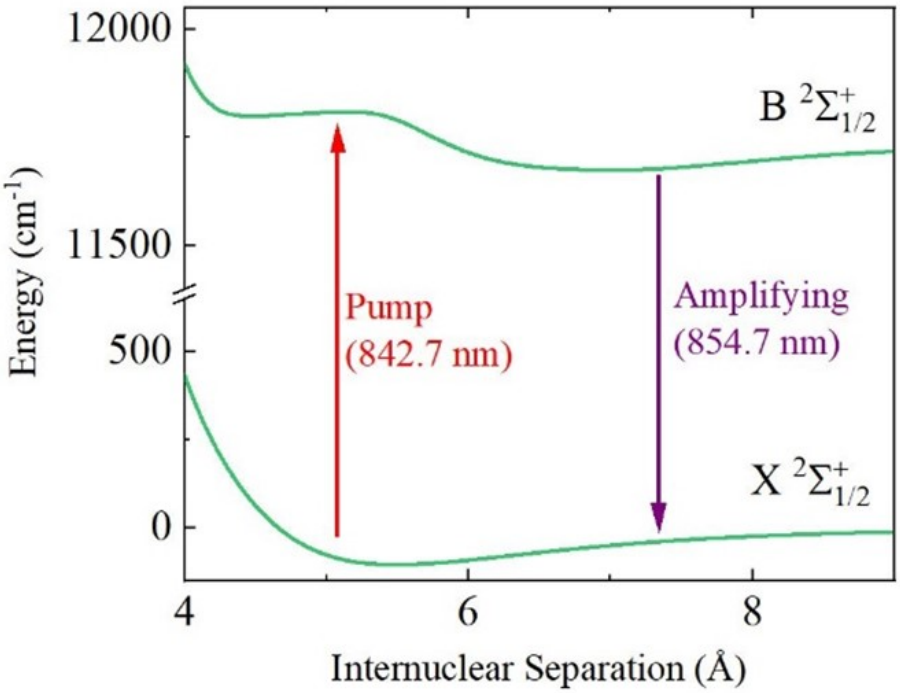

Figure 3.9: Interatomic potential curve for a Cs-Xe pair. The red and purple arrows indicate where the pump and amplification occurs.

The potential curve is also shown in Figure 3.9. The blue and purple arrows indicate where the blue and red satellite transition occurs. The lower state has a van der Waals minimum of 105.8 cm^{-1} while the upper state has two local minima. In a semiclassical point of view, the potential difference can be used to determine the transition wavelength with a technique called quasi-static line broadening [19]. When the potential difference is at extreme, the transition occurs. Dhiflaoui *et al.* [35] performed *ab initio* calculation of the Cs-Xe interatomic potential curve and expected that transition occurs at the wavelength of approximately 842 nm and 854 nm from the $B^2\Sigma^+_{1/2}$-$X^2\Sigma^+_{1/2}$

potential difference.

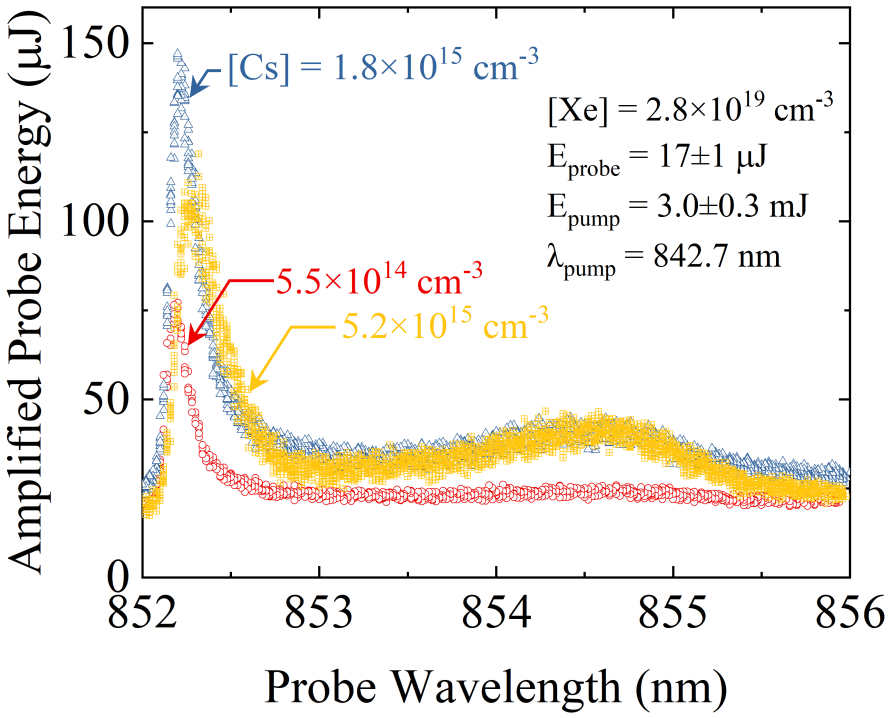

Figure 3.10: The amplified probe energy versus the probe wavelength when the Cs-Xe cell is pumped optically at the blue satellite.

The gain spectrum of the Cs-Xe cell for different Cs number densities is shown in Figure 3.10. The Cs number density is varied from 5.5×10^{14} cm^{-3} to 5.2×10^{15} cm^{-3} corresponding to the gas temperature range between 453-493 K. The pressure of xenon buffer gas is 800 Torr and the corresponding gas number density is 2.8×10^{19} cm^{-3}. The pump energy and the wavelength are 3.0 mJ and 842.7 nm which is the peak of the blue satellite of Cs-Xe.

While the spectrum near the D_2 line looks similar to the case of CsAr, the red satellite is prominent at 854.7 nm. Compared to the absorption spectrum, the red satellite is visibly distinct in the excitation spectrum because the red wing transition is suppressed in the gain spectrum. As already discussed for the blue wing of the D_2 line in Section 3.2, the red wing is the result of bound-free transition between the $A^2\Pi_{3/2}$ and $X^2\Sigma^+_{1/2}$. In the gain spectrum, the contribution of bound-free transition in the gain spectrum in Figure 3.10 is negligible since the time delay is set to 1 ns which is much smaller than the kinetic energy relaxation time of the transient molecule.

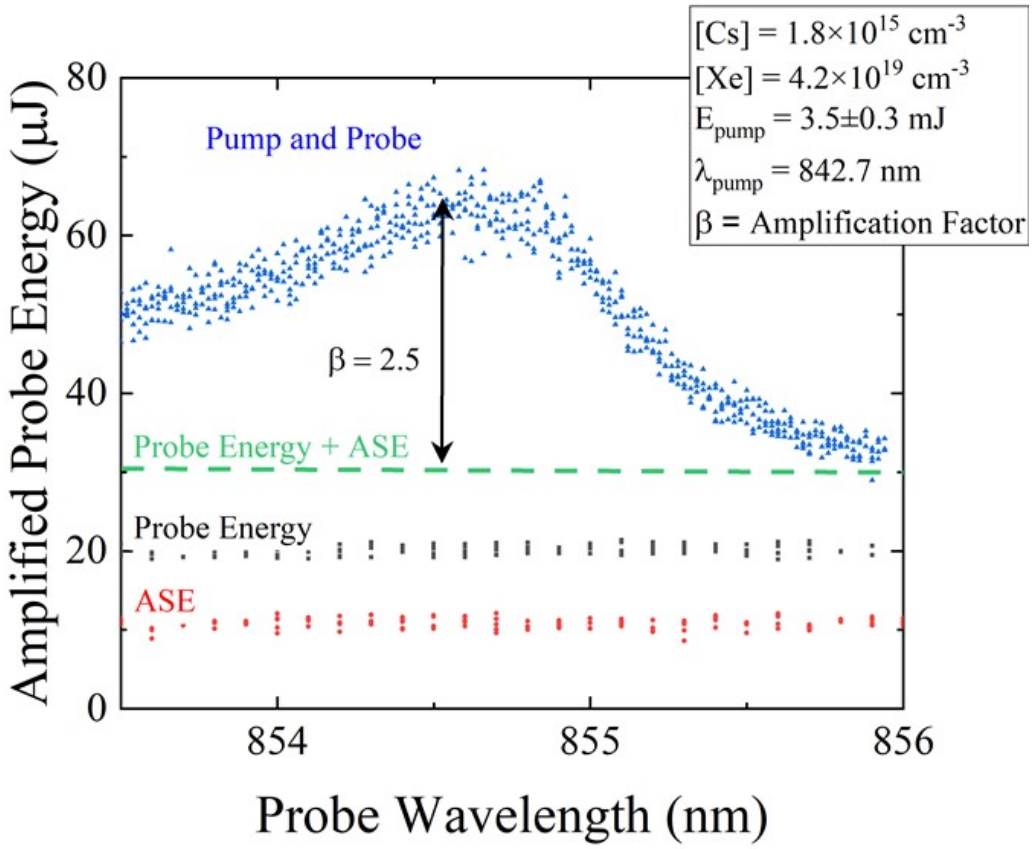

Figure 3.11: A magnified view of the gain spectrum of the Cs-Xe gas mixture showing the amplification occurs in the red satellite of the D_2 line.

Figure 3.11 shows a magnified view of the gain spectrum of the gas cell between 853.5 nm to 856 nm when the blue satellite is optically pumped. The Xe pressure is 1200 Torr and the corresponding Xe number density is 4.2×10^{19} cm^{-3}. The probe energy and ASE are shown in the figure to indicate the transparency energy for the spectrum. The transparency line where two values are added is also shown as a purple color, clearly indicating the red satellite is being amplified.

In order to double-check whether the red satellite is amplified by the probe energy, competition between ASE and the lasing is studied in Figure 3.12. Since both ASE and lasing in the red satellite extract energy from the excited Cs-Xe pairs, when one dominates, the other has to be suppressed. The spectrum is taken by a compact spectrometer (SPM, Photon Control). The resolution of the spectrum is approximately 1 nm in the spectral range. The fiber attached to the spectrometer probes the scattered light from Detector

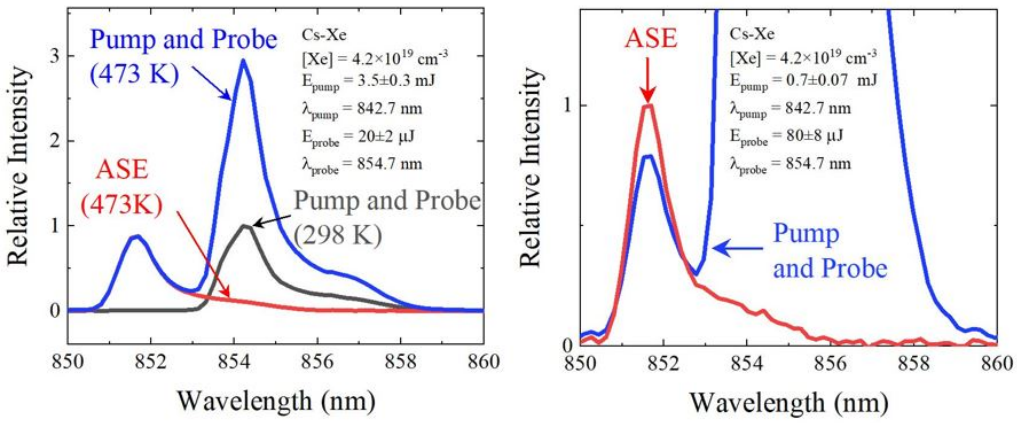

Figure 3.12: The spectrum of the output probe pulse. The black curve is obtained when the gas cell is at room temperature where the medium does not have gain. The red curve is obtained when only the pump pulse is introduced. The blue curve is taken when both pump and probe pulses are introduced showing both ASE and amplification of the probe pulse. (left) The spectrum taken when the probe pulse energy is low and the pump pulse energy is high (right) The spectrum taken when the probe pulse energy is high and the pump pulse energy is low.

3 which collects the probe pulse that passed the gas cell.

The two spectra are taken for two different pump and probe energies. The black line in the left spectrum shows the probe energy spectrum when the gas is at room temperature, which indicates that the cell does not have gain. The red curve is the spectrum when the pump beam is introduced at the gas temperature of 473 K showing the ASE of the D_2 line. The blue curve is taken with the introduction of both the pump and probe beams. There is no clear distinction in ASE between the blue and red curves. By increasing the probe energy by four times and lowering the pump energy five times for the figure on the right, the ASE is shown to be suppressed when lasing occurs. This is a clear indication that amplification is occurring in the red satellite.

The efficiency curve can also be drawn by changing the pump energy as shown in Figure 3.13. The efficiency is calculated by considering the amplified probe energy excluding the ASE energy and dividing it by the input pump energy. The curve shows the threshold energy is 1.3 mJ and the maximum efficiency is 0.9 %.

In Section 3.4, the Franck-Condon calculation will be conducted to simulate the experimental curve responsible for the free-free molecular transition.

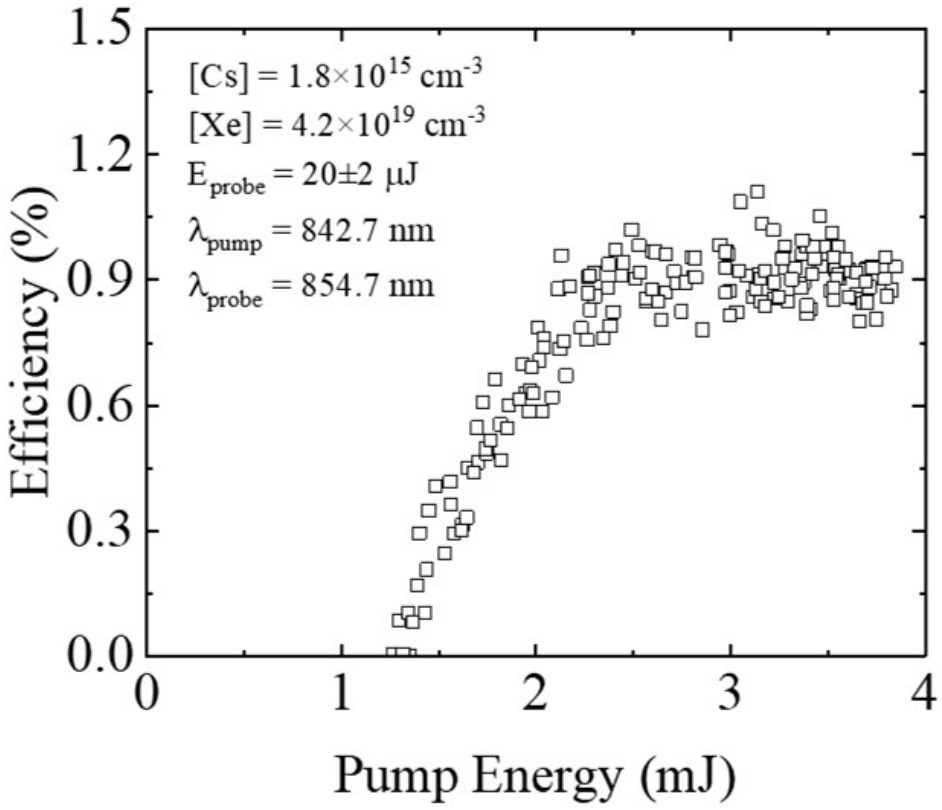

Figure 3.13: Efficiency curve for the free-free amplifier. The experimental condition is shown in the plot.

Before leaving this section, it should also be discussed that the gain near the D_2 line in the wavelength between 852.1 nm and 853 nm for both Cs-Ar and Cs-Xe pairs can be considered as a result of the free-free molecular transition. As discussed in Section 3.2, the broadening of the gain spectrum is not the result of the pressure of resonance broadening of $6^2P_{3/2}$ state. It is a consequence of the transition between long-ranged free molecular states of $B^2\Sigma^+_{1/2}$ and $X^2\Sigma^+_{1/2}$. However, there is a difficulty to perform the Franck-Condon calculation for the long-ranged free molecular states because the long-ranged potential curves do not have distinctive features as it approaches the Cs atomic resonance state at the infinity internuclear distance. Thus, the calculation will be performed for the red satellite of Cs-Xe.

3.4 Franck-Condon Calculation

In order to study the origin of the red satellite, a quantum-mechanical calculation will be conducted. The technique used in this work is the same as the work by Hewitt [36]. The free wavefunctions are obtained by the Numerov-Cooley method from the given potential curves [37].

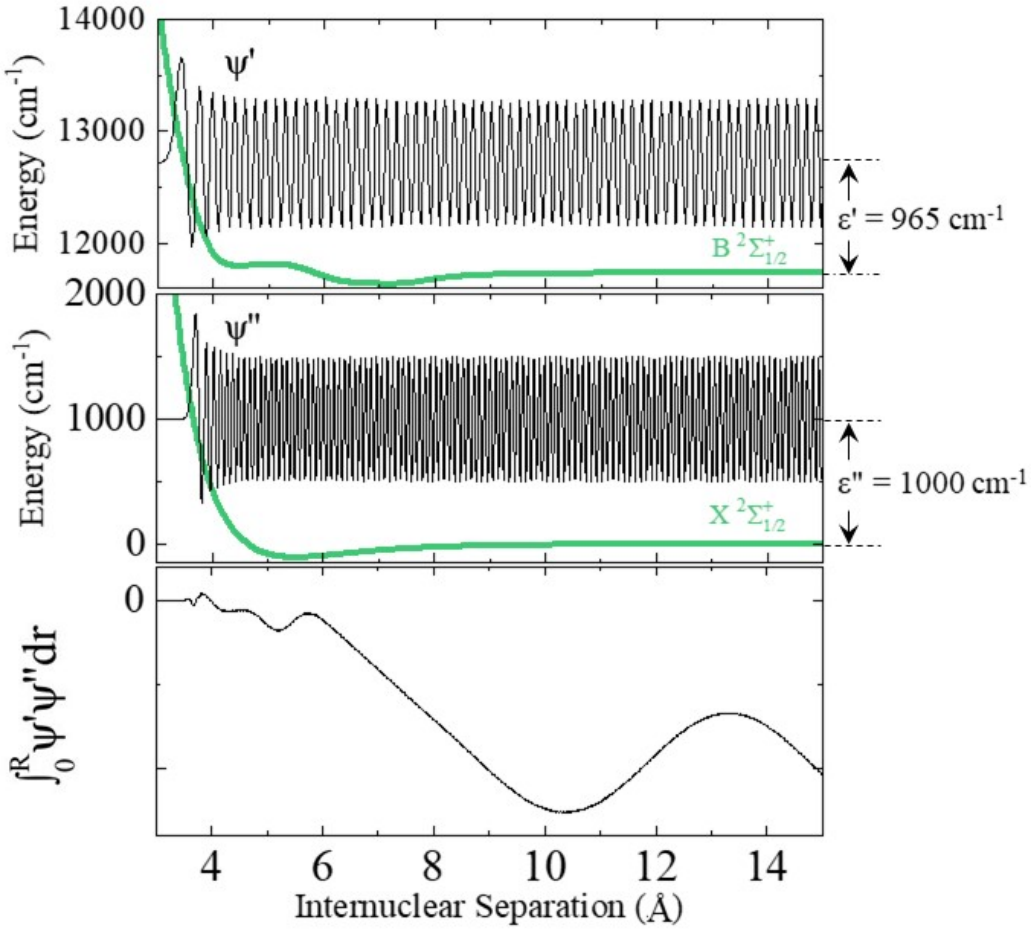

Figure 3.14: (top and middle) Representative wavefunctions responsible for stimulated emission at 854.7 nm. (bottom) Overlap integrals of the wavefunctions.

The representative wavefunctions are shown in Figure 3.14. The kinetic energies of the upper and lower states are chosen as 1000 cm^{-1} in the $X^2\Sigma^+_{1/2}$ state and 965 cm^{-1} in the $B^2\Sigma^+_{1/2}$ state, respectively, so that the overlap integral can represent the behavior of the peak of the red satellite which is approximately 35 cm^{-1} apart from the D_2 line transition. The bottom plot

in Figure 3.14 is the overlap of these two wavefunctions. The overlap integral develops at the internuclear separation of 6-9 Å. As the Franck-Condon factor which is square of the overlap integral determines the transition probability, the electronic transition with the energy lowered by 35 cm^{-1} compared to the D_2 line occurs at the internuclear separation of 6-9 Å. This interatomic spacing is where the shallow well is located in the $B^2\Sigma^+_{1/2}$ state. The blue satellite is thought to occur at the internuclear spacing of approximately 5.5 Å where another shallow well is located. The small feature in the potential curve results in the dramatic change in the resulting spectrum because it allows for the potential difference to be extremum in the region. It should be noted that the depths of the wells of the $B^2\Sigma^+_{1/2}$ and $X^2\Sigma^+_{1/2}$ states are smaller than the mean value of the kinetic energies of atoms which is 329 cm^{-1} in 473 K. As a result, the fraction of the bound molecule is negligible compared to the fraction of the free atoms in the energy space.

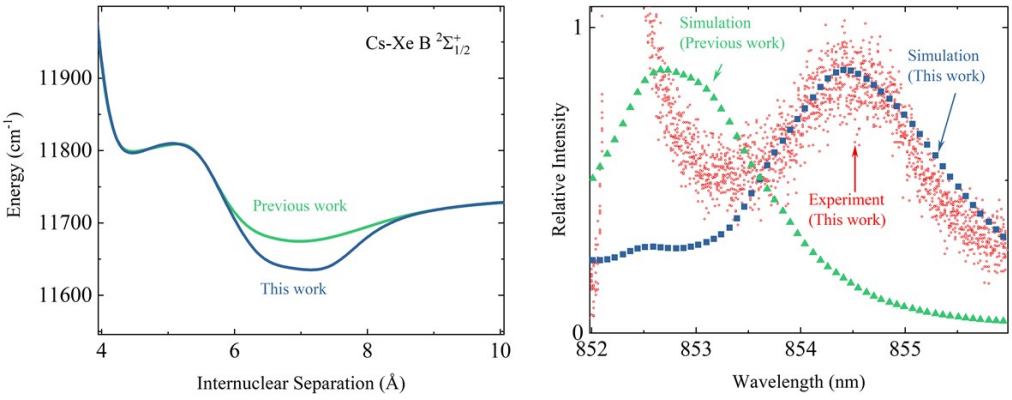

Figure 3.15: (left) Potential curves for the $B^2\Sigma^+_{1/2}$. The green line is a previous work by Hewitt. The blue line is a modified curve to fit the experimental result. (right) Comparison of the simulation with the experimental spectrum.

Then, the emission spectrum can be obtained from the expression [38],

$$k(\lambda) \propto \Sigma_{J=0}^{J_{max}} \int_{\epsilon'_J=0}^{\epsilon'_{max}} \int_{\epsilon''_J=0}^{\epsilon''_{max}} (2J+1) exp(\frac{-\epsilon'_J}{kT}) \mid < \psi'(\epsilon'_J) \mid \psi''(\epsilon''_J) > \mid^2 \quad (3.1)$$

where λ is wavelength, J is rotational quantum number, k is Boltzmann con-

stant, T is temperature, ψ' and ψ'' are upper and lower state wavefunctions, and ϵ' and ϵ'' are energies in the upper and lower states. The last term which is a square of the integral overlap is called a Franck-Condon factor.

The right spectrum in Figure 3.15 shows the comparison between simulation and experimental result. The overlap integral is obtained for the interatomic spacing between 6-9 Å with the increment of 0.01 Å. The lower and upper state kinetic energies are 25-3000 cm^{-1} by the increment of 1 cm^{-1}. The rotational quantum numbers are 1-100 by the increment of 2. Assuming the system is in the thermal equilibrium, the Boltzmann factor weights the Franck-Condon factors. The temperature is 473 K which is the same in the experiment. The green curve is obtained from the potential curve with the same color in the left figure. A discrepancy to the experimental data can be adjusted by changing the depth of the well of $B^2\Sigma^+_{1/2}$ potential using the same technique used in [36]. The modified potential and spectrum are shown as blue curves on the left in Figure 3.15. Changing the depth of the well shifts the peak to the red side of the D_2 line further, which makes a good agreement with the experimental result.

The experiment and theoretical work indicate that the red satellite amplifier may be regarded as a free-free amplifier in which the amplification process occurs as a free-free molecular transition. However, it should be noted that the potential curve of the $A^2\Pi_{3/2}$ state shares similar features in the shape with the $B^2\Sigma^+_{1/2}$ state at 6-9 Å [35]. Although the $A^2\Pi_{3/2}$ and $B^2\Sigma^+_{1/2}$ states cannot be regarded as bound states at the internuclear separation of 6-9 Å due to the small value of the potential depth ($\sim$100 cm^{-1}), it should be considered that $A^2\Pi_{3/2}$ state may be regarded as a quasi-bound state. A further study is required to obtain the exact ratio of the free states and the quasi-bound state responsible for the optical amplification in the red satellite of the D_2 line. Nevertheless, because the well depth of the $A^2\Pi_{3/2}$ ($\sim$500 cm^{-1}) is comparable to the value of kT (328 cm^{-1}) at 473 K, the state cannot form strong bound states. In conclusion, optical amplification of the red satellite of the D_2 line depends mainly on free molecular interaction on both pumping and amplifying process.

CHAPTER 4

MICROPLASMA MERCURY LAMP

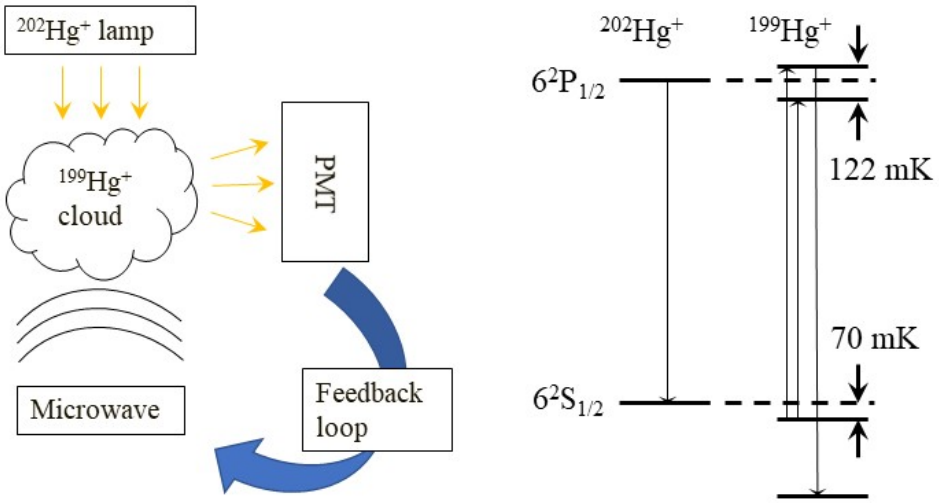

Figure 4.1: (left) A schematic description of the operation of a mercury ion clock. (right) Relative energy levels of $^2P_{1/2}$ and $^2S_{1/2}$ states of $^{202}Hg^+$ and $^{199}Hg^+$ and optical pumping mechanisms in $^{199}Hg^+$ when photons emitted by $^{202}Hg^+$ are absorbed by $^{199}Hg^+$. The partial energy diagram is reproduced from [39].

The purpose of the mercury ion lamp is to provide the 194.2 nm radiation to drive a mercury ion atomic clock. The mercury ion clock has shown better performance in accuracy compared to the cesium and rubidium atomic clock [40]. Furthermore, the insensitivity to the external magnetic field and the large mass of a mercury ion make the mercury ion clock more competitive to other atomic clocks. The technology is expected to be an essential part of the next generation of Global Positioning System (GPS). The 194.2 nm radiation is a transition between mercury ion states from $6^2P_{1/2}$ to $6^2S_{1/2}$ which is the ground state of Hg^+. A schematic in Figure 4.1 describes how the ion trap and the lamp work as an ion clock. Once the $^{199}Hg^+$ cloud is prepared in the ion trap, the $^{202}Hg^+$ lamp optically pumps the ion cloud so

that the $^{199}Hg^{+}$ is prepared for the clock transition. This process is possible because the hyperfine splitting by nuclear spin occurs only for $^{199}Hg^{+}$. The diagram in the middle in Figure 4.1 reveals the energy levels of the two isotopes. The right figure shows how the $^{199}Hg^{+}$ ions are prepared for the ion clock transition. When the $^{199}Hg^{+}$ ions are optically pumped by the photons emitted by $^{202}Hg^{+}$, they are eventually populated into the F = 0 sublevel of the ground state. Spontaneous emission from the ion cloud is detected by the photomultiplier tube (PMT). Once the optical pumping is done, a microwave that has a frequency of 40.5 GHz pumps the ion cloud to the upper state of the clock transition. The feedback loop finds the largest signal sweeping the frequency of the microwave. The frequency at the largest signal is utilized to determine a second.

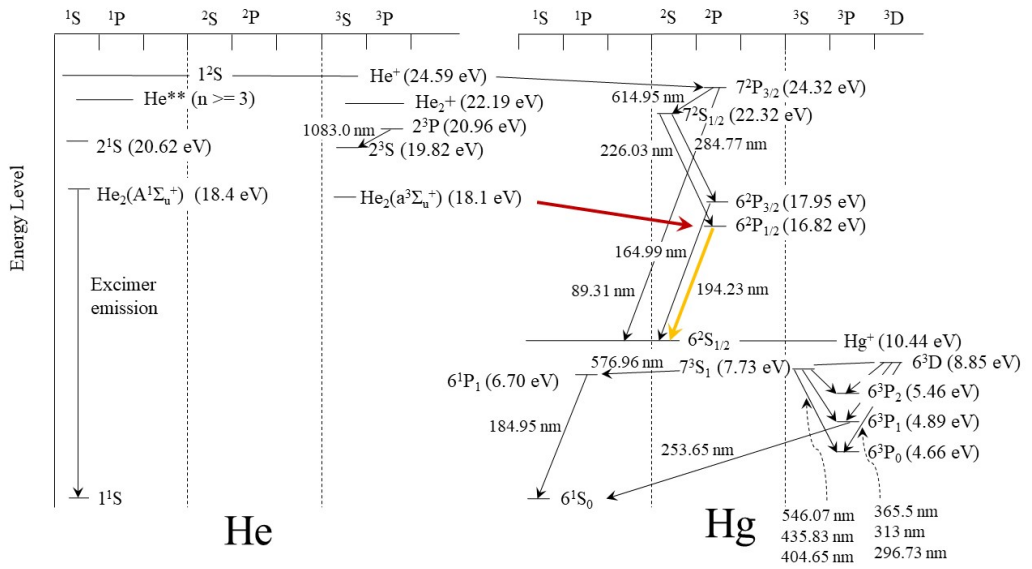

Figure 4.2: Partial energy diagram of helium and mercury.

The upper state, $6^2P_{1/2}$, is located 6.38 eV above the ground state of the mercury ion and the ionization energy of the mercury neutral atom is 10.44 eV. Because the energy required to populate the state is 16.82 eV in total, populating the $6^2P_{1/2}$ state is not favored by electron impact ionization and excitation since the typical average electron temperature is a few eV in microplasmas. However, the present work proposes a kinetic pathway that can access the upper state of 194.2 nm radiation by penning ionization of helium molecular metastable.

Figure 4.2 is a partial energy level diagram of helium and mercury. In

helium, states whose primary quantum number is 2 are shown in the diagram. Each state is converted to the helium excited dimer state by colliding with helium neutrals in the presence of another helium neutral atom as a recoil gas. The $A^1\Sigma_u^+$ state emits excimer radiation whose wavelength ranges from 60-90 nm. On the other hand, the $a^3\Sigma_u^+$ state is metastable which has a long radiative lifetime larger than several seconds [41]. It is also known that the upper states of the excimer quench to the $a^3\Sigma_u^+$ state quickly [42]. Thus, the primary excimer source will be the $a^3\Sigma_u^+$ state. The red arrow indicates the penning ionization process that ionizes and excites the ground state of the mercury atom to the upper state of the 194.2 nm transition. In the energy diagram of Hg, prominent radiative transitions are indicated. For mercury neutral, the 253.7 nm and 185.0 nm are readily observed. For the mercury ion, several significant transitions are presented in the diagram. The desired radiative transition of 194.2 nm is indicated by a yellow arrow and is caused by a transition between the $6^2P_{1/2}$ state and the $6^2S_{1/2}$ state.

In this chapter, the realization of the mercury ion lamp and the validation of the kinetic pathway will be presented. The structure of the lamp will be shown in Section 4.1. A description of the zero-dimensional kinetic model will be discussed in Section 4.2. In Section 4.3, the results from experiments as well as computational simulation will be presented together to validate the kinetic path of the He-Hg plasma system. Section 4.4 will discuss the lamp failure mechanism as well as enhancement of the lifetime of the lamp.

4.1 Lamp Structure and Characteristics

A structure of the microplasma mercury ion lamp is shown in Figure 4.3. The lamp is largely comprised of a window, a spacer, a bottom plate, and a gas feeding line. Each part is made with quartz while the window has transmittance more than 90% at 194.2 nm. These parts are sealed with glass frit which is specially developed for quartz sealing to minimize gas permeation through the seal. The top-right figure is a cutaway view of the lamp that shows the dimension of each part. There are two different sizes of the cavities which are 1 mm and 0.6 mm in diameter. The depths of the cavities are 0.5 mm. The thickness of a window, a spacer, and a bottom plate is 1 mm. The overall size of the lamp body is 12 mm by 12 mm in length

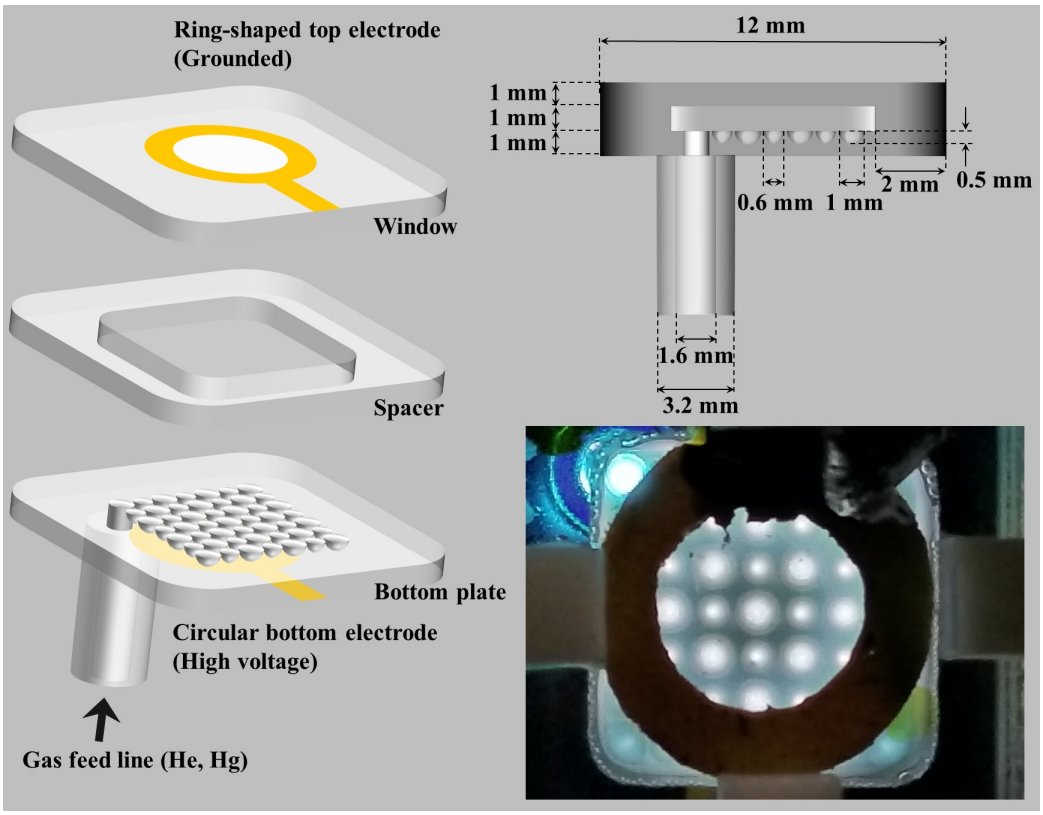

Figure 4.3: (left) A schematic that shows the lamp structure is mainly segmented by four different parts which are a window, a spacer, a bottom plate, and a gas feeding line. (top-right) A side view of the lamp when it is assembled. The dimensions are indicated by arrows. (bottom-right) A photo of the lamp in operation. The pressure of He buffer gas is 300 Torr and ^{202}Hg isotope is fed to the device. The lamp is driven with a 137 kHz HV pulser.

and width while the height is 3.5 mm including the thickness of the glass frit seal. The inner and outer diameters of the gas feeding line are 1.6 and 3.2 mm, respectively. The gas feeding line is used to feed the mercury vapor and the helium buffer gas. The gold electrodes are pasted and baked as a ring shape for the window and a circular shape for the bottom plate. A photo at the bottom-right corner is taken when the lamp is mounted on a customized holder and operated with a 137 kHz bipolar pulser. The lamp is filled with 300 Torr of He and ^{202}Hg isotope. The different sizes of the cavity discharges are clearly shown in the photo. The bright spot at the top-left corner is the gas feeding line.

Figure 4.4. is a circuit diagram to drive and test the lamp. The high volt-

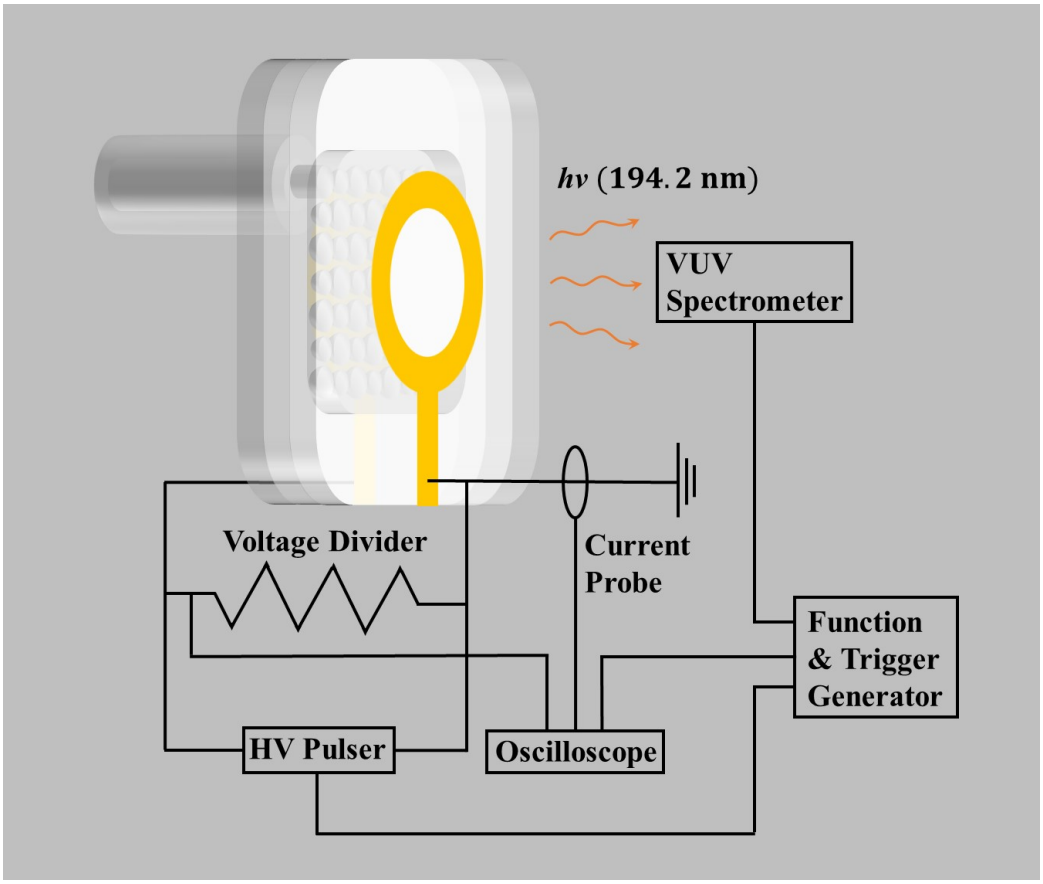

Figure 4.4: An experimental setup that measures waveform of the voltage, current, and emission of the microplasma mercury lamp.

age pulser is comprised of a DC voltage supply (EPR 1015, Matsusada) and a pulse generator (PVX-4110, Directed Energy). The voltage is applied to the circular electrode on the bottom plate while the ring-shaped electrode on the window is grounded. The pulse width and the amplitude of the voltage are controlled by the function generator. The voltage and current measured by the voltage probe (CT4024, Cal Test Electronics) and the current probe (2877, Pearson) and the waveform is taken with the oscilloscope. The vacuum ultraviolet (VUV) spectrometer (SP2758, Princeton Instrument) used in the experiment is equipped with the ICCD camera (PI-MAX 4, Princeton Instrument). The spectrometer is purged with nitrogen for VUV transmission. The ICCD camera is triggered by the same function generator to take a temporally resolved spectrum.

4.2 Zero-Dimensional Kinetic Model

For a better understanding of the He-Hg plasma system, a zero-dimensional kinetic simulation freeware (ZDPlasKin v. 2.0) [43] is adopted. The freeware is incorporated with an ordinary differential equation solver (VODE) [44] and a Boltzman equation solver (Bolsig+) [45] to simulate non-thermal plasmas. All the species shown in the partial energy diagram in Figure 4.2 were included in the model. The detailed information of the cross sections and rate constants used in the model are listed in Appendix A. For helium, only three excited states whose primary quantum number is 2 (2^3S, 2^1S, and 2^3P) are included "as is" while the highly excited states with the primary quantum number more than 3 are lumped into He^{**}. In the case of mercury, six excited states of mercury neutrals and four excited states of mercury ions are considered in order to simulate the kinetic pathway properly. In Section 4.2.1, the reactions considered in the kinetic model will be described.

4.2.1 Collision Kinetic

Electron Impact Excitation

The rate constants of electron impact excitation and ionization were obtained by Bolsig+.

$$e + He \leftrightarrow e + He^*$$
$$e + He^* \leftrightarrow e + He^{*\prime}$$
$$e + Hg \leftrightarrow e + Hg^*$$
$$e + Hg^* \leftrightarrow e + Hg^{*\prime}$$
$$e + Hg^+ \leftrightarrow e + Hg^{+*}$$

X^* includes all the excited species of X. $X^{*\prime}$ represents excited species which are different from X^*. De-excitation is also included by detailed balancing as the left arrow indicates. The excitation to the $7^2S_{1/2}$ and $7^2P_{3/2}$ is not included because of the absence of data. However, as the total energy required to populate these states is above 22 eV, the electron impact excitation will not contribute much to the result.

Electron Impact Ionization

Similar to the case of electron impact excitation, the rate constants are derived by solving the Boltzmann equation.

$$\begin{aligned}
\mathrm{e} + \mathrm{He} &\rightarrow \mathrm{e} + \mathrm{e} + \mathrm{He}^+ \\
\mathrm{e} + \mathrm{He}^* &\rightarrow \mathrm{e} + \mathrm{e} + \mathrm{He}^+ \\
\mathrm{e} + \mathrm{He}_2^* &\rightarrow \mathrm{e} + \mathrm{e} + \mathrm{He}_2^+ \\
\mathrm{e} + \mathrm{Hg} &\rightarrow \mathrm{e} + \mathrm{e} + \mathrm{Hg}^+ \\
\mathrm{e} + \mathrm{Hg}^* &\rightarrow \mathrm{e} + \mathrm{e} + \mathrm{Hg}^+
\end{aligned}$$

Heavy Particle Collision

The excited helium and helium ion collide with a helium neutral atom in the presence of another helium atom to form a helium excimer and a helium dimer ion, respectively.

$$\begin{aligned}
\mathrm{He}^* + \mathrm{He} + \mathrm{He} &\rightarrow \mathrm{He}_2^* + \mathrm{He} \\
\mathrm{He}^+ + \mathrm{He} + \mathrm{He} &\rightarrow \mathrm{He}_2^+ + \mathrm{He}
\end{aligned}$$

In atmospheric pressure plasmas, the conversion into the dimer form occurs very fast. Dissociative recombination becomes a dominant recombination mechanism for high pressure plasmas due to this reaction.

The mercury ion is converted to a mercury dimer in the same manner.

$$\mathrm{Hg}^+ + \mathrm{Hg} + \mathrm{He} \rightarrow \mathrm{Hg}_2^+ + \mathrm{He}$$

The penning ionization by excited species of helium and mercury is included.

$$\begin{aligned}
\mathrm{He}^* + \mathrm{He}^* &\rightarrow \mathrm{He}^+ + \mathrm{He} + \mathrm{e} \\
&\rightarrow \mathrm{He}_2^+ + \mathrm{e} \\
\mathrm{He}^* + \mathrm{He}_2^* &\rightarrow \mathrm{He}^+ + \mathrm{He} + \mathrm{He} + \mathrm{e} \\
&\rightarrow \mathrm{He}_2^+ + \mathrm{He} + \mathrm{e} \\
\mathrm{He}_2^* + \mathrm{He}_2^* &\rightarrow \mathrm{He}^+ + \mathrm{He} + \mathrm{He} + \mathrm{He} + \mathrm{e} \\
&\rightarrow \mathrm{He}_2^+ + \mathrm{He} + \mathrm{He} + \mathrm{e} \\
\mathrm{Hg}^* + \mathrm{Hg}^* &\rightarrow \mathrm{Hg}^+ + \mathrm{Hg} + \mathrm{e} \\
&\rightarrow \mathrm{Hg}_2^+ + \mathrm{e}
\end{aligned}$$

The penning ionization process by helium excimer that ionizes and excites a mercury neutral is considered to produce $6^2\mathrm{P}_{1/2}$ and $6^2\mathrm{P}_{3/2}$.

$$\begin{aligned} He_2^* + Hg &\rightarrow He + He + Hg^+(6^2P_{1/2}) + e \\ &\rightarrow He + He + Hg^+(6^2P_{3/2}) + e \end{aligned}$$

Kurunczi *et al.* [29] reported that energy transfer from He_2^* to O_2, N_2, and H_2 produces atomic radiations from O, N, and H, respectively. Based on the total enegy required for the radiation, they estimated the energy contained in the excimer is 12.40-21.38 eV. In the case of mercury, $Hg^+(6^2P_{1/2})$ and $Hg^+(6^2P_{3/2})$ states require 16.82 and 17.95 eV, respectively, which are in the range of their approximation.

Charge transfer from a helium ion to the $7^2P_{3/2}$ state of a mercury ion was also included.

$$He^+ + Hg \rightarrow He + Hg^+(7^2P_{3/2})$$

The He-Hg plasma system was studied as a visible laser system emitting 615 nm, a transition from $Hg^+(7^2P_{3/2})$ to $Hg^+(7^2S_{1/2})$ [46]. Charge transfer from helium ion is the main mechanism to pump the laser. This reaction was included in the kinetic model because it could contribute to populating the upper state of 194.2 nm by subsequent quenching from the $Hg^+(7^2P_{3/2})$ state.

Recombination

The dominant recombination mechanism for helium is dissociative recombination due to its large number density.

$$He_2^+ + e \rightarrow He^* + He$$

The two types of three-body recombinations, collsional-radiative and neutral-stabilized, are also considered.

$$\begin{aligned} He_2^+ + e + e &\rightarrow He^* + He + e \\ He_2^+ + He + e &\rightarrow He^* + He + He \\ He^+ + e + e &\rightarrow He^* + He + e \end{aligned}$$

Due to the low number density of mercury ($\sim 10^{13}$ cm^{-3} at 300 K), the collisional-radiative recombination of a mercury ion was also considered.

$$Hg^+ + e + e \rightarrow Hg^* + e$$

The recombination of ion dimer is also included.

$$Hg_2^+ + e \rightarrow Hg^* + He$$
$$Hg_2^+ + e + e \rightarrow Hg^* + Hg + e$$
$$Hg_2^+ + He + e \rightarrow Hg^* + Hg + He$$

Ambipolar Diffusion

Loss of the charged species by ambipolar diffusion to the wall is considered.

$$R \approx \frac{D_a}{\Lambda^2} \approx \frac{\mu_\circ k T_e}{q} \frac{P_{He}}{760} \frac{1}{\Lambda^2} \tag{4.1}$$

D_a is ambipolar diffusion coefficient. $\mu_\circ$ is an ion mobility at 300 K and 760 Torr of helium. k is the Boltzman constant. T_e is electron temperature. q is a unit charge. P_{He} is the pressure of helium in Torr. Λ is the characteristic diffusion length. For spherical geometry,

$$\Lambda^2 \approx (\frac{r}{\pi})^2 \tag{4.2}$$

r is the radius of the sphere. It is also assumed that the charged species that are lost by diffusion to the wall are quickly converted to the ground state of neutral species by recombination at the wall by having the reaction constants with a large value.

Spontaneous Emission

Radiative transitions are indicated by arrows in Figure 4.2. At temperature larger than 310 K, the mercury number density is high enough to consider radiation trapping. The imprisonment effect is considered by multiplying a trap factor, g, to the spontaneous emission coefficient [47].

$$g \approx 1.15(\frac{\lambda_\circ}{3\pi^2 d} \frac{n_{He}}{n_{Hg}})^{1/2} \tag{4.3}$$

Joule heating by elastic collision of electrons with neutrals has been neglected letting the gas temperature remain constant.

4.2.2 Equivalent Circuit

The microplasma mercury lamp is based on the DBD plasma. Because of the quartz dielectric between the electrode and the gas, the voltage drop in

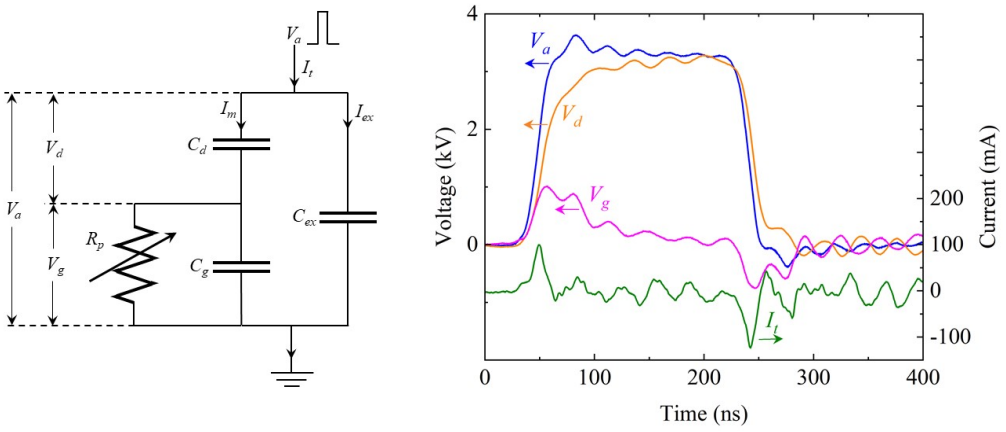

Figure 4.5: (left) The equivalent circuit model for microplasma mercury lamp. C_d is capacitance of the dielectric barrier of the lamp. C_g is the capacitance of the gas. C_{ex} is capacitance of the electrode painted on the spacer area for connection to the external circuit. R_p is variable resistance of the plasma. $V_a(t)$ is the applied voltage provided by the pulse generator, $V_d(t)$ is the voltage drop in the dielectric barrier of the lamp, $V_g(t)$ is the voltage drop in the gas. $I_t(t)$ is the total current. $I_{ex}(t)$ is the displacement current through C_{ex}. $I_m(t)$ is the current flowing into the microplasma mercury lamp. (right) The waveform of $V_a(t)$, $V_d(t)$, $V_g(t)$, and $I_t(t)$. $V_a(t)$ and $I_t(t)$ are obtained experimentally while $V_d(t)$ and $V_g(t)$ are calculated.

the gas does not match the voltage provided by the pulse generator. This is not only because the voltage is shared by the gas and the quartz based on the capacitance, but also because the charge accumulated on the dielectric compensates for the applied voltage [48], [49]. The gap voltage has been analyzed by Liu and Neiger [50] with a simple electrical circuit model for a plane-parallel DBD driven by nanosecond pulses. The accumulated charge ceases the discharge and is released when the voltage falls at the end of the unipolar pulse. As a result, two peaks of plasma current, one when the voltage rises and another when it falls, are observed in each pulse for DBD. Although the microplasma mercury lamp used in this work has a relatively complicated structure compared to the plane-parallel case, a similar circuit model is implemented to obtain the waveform of the gap voltage as shown in Figure 4.5. The notations for the components are listed in the caption of Figure 4.5. The circular and ring-shaped of the electrodes are approximated to the plane-parallel case. As a result, the total capacitance of the lamp is represented by a series of two capacitors, C_d and C_g. C_d represents the total capacitance of the two dielectric barriers of the lamp. A variable resistor, R_p,

is in parallel to the C_g. The resistance is assumed to be infinite when the gas discharge does not occur while the resistance decreases when the discharge happens letting the conduction current flow through it. C_{ex} is added in this work to compensate for the external capacitance due to the extended electrode drawn on the periphery of the lamp surface where the spacers are located. The extended electrode is necessary for the electrical connection to the external circuit that drives the lamp. As already discussed above, the voltage applied in the gas is not equivalent to the voltage provided by the pulse generator because of the dielectric barriers. The gap voltage, $V_g(t)$, can be calculated from the values of $V_a(t)$, $I_t(t)$, C_d, and C_g. When the discharge does not occur, the voltage drop in the dielectric barrier, $V_d^\circ(t)$, can be obtained as

$$V_d^\circ(t) = \frac{C_g}{C_d + C_g} V_a(t) \tag{4.4}$$

When the gas discharge occurs, there is a change in V_d

$$\Delta V_d(t) = \frac{1}{C_d} \int_0^t \Delta I_t(\tau) d\tau \tag{4.5}$$

where $\Delta I_t(t)$ is a change in total current when the the discharge occurs compared to when it does not. To obtain the waveform of the total current when discharge does not occur, the peak voltage was chosen as the value that is lower than the breakdown voltage, but higher than the sustaining voltage. The lamp was driven with a certain voltage lower than the breakdown voltage first. Then, the voltage was raised until the breakdown occurs. Finally, the voltage was lowered to the original voltage when the gas discharge still occurs. Also, $\Delta I_t(t)$ is the same as $\Delta I_m(t)$ as C_{ex} is constant regardless of the occurrence of the gas discharge. The voltage drop in the dielectric barrier when discharge occurs is

$$V_d(t) = V_d^\circ(t) + \Delta V_d(t) \tag{4.6}$$

The value for $V_g(t)$ can be obtained from a simple subtraction.

$$V_g(t) = V_a(t) - V_d(t) \tag{4.7}$$

The resulting waveform is shown in the right plot in Figure 4.5. $V_a(t)$ and $I_t(t)$ are obtained experimentally and $V_d(t)$ and $V_g(t)$ are calculated from the

equations above. The gap voltage, $V_g(t)$, shows a double-pulsing behavior in each unipolar pulse.

4.3 Result

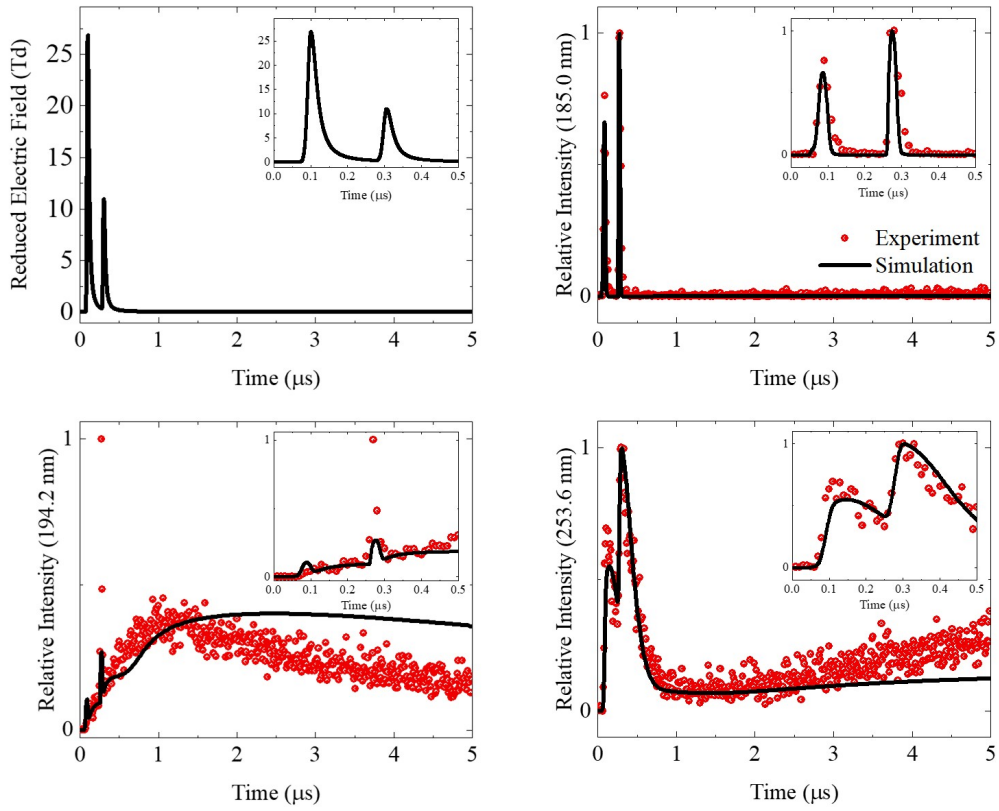

Figure 4.6: (top-left) The waveform of the voltage pulse made artificially based on the equivalent circuit model in 4.5. The Gauss-Lorentzian shape is implemented. The peak voltage for the first pulse is 1000 V while the peak value for the second pulse is adjusted based on the emission waveform. (else) The red dotted circle is a temporally resolved spectrum of 185.0 nm, 194.2 nm and 253.7 nm that is taken experimentally while the black curve is a kinetic simulation showing that the trend of the waveform resembles the experimental result.

A comparison between experimental and simulated result is shown in Figure 4.6. The helium pressure is 600 Torr and the amplitude and the pulse width of the voltage pulse are 3 kV and 200 ns, respectively, as shown in Figure 4.5. The PRF is 5 kHz in both experiment and simulation. Since the

simulation does not have spatial dimensions, the polarity of the gas voltage obtained in Section 4.3.2 is ignored resulting in the waveform in the top-left corner in Figure 4.6. The amplitude of the first pulse is 1,000 V as deduced from the equivalent circuit model while the amplitude of the second pulse is adjusted as 400 V to match the simulated waveforms to the experimental ones. The plot shows the corresponding reduced electric field values on the axis. The steady-state is achieved after five periods.

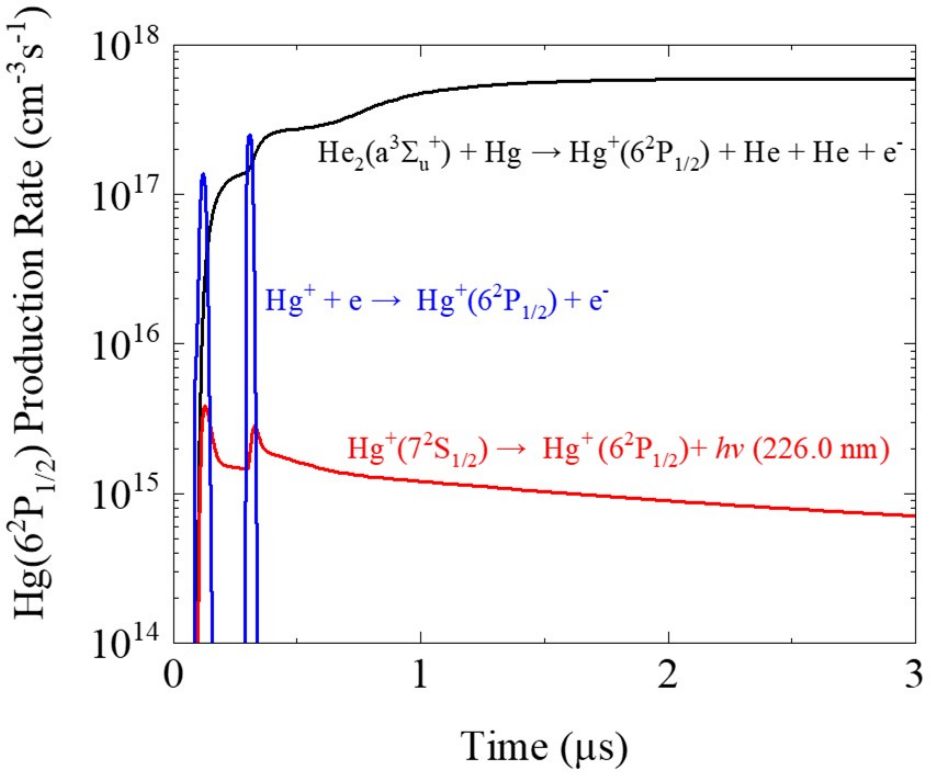

Figure 4.7: The production rate of the Hg $6^2P_{1/2}$ state by three different mechanisms.

The three other plots in the figure show experimental and simulated waveform of three different atomic lines of mercury. Two mercury neutral lines, 185.0 nm (6^1P_1 to 6^1S_0) and 253.7 nm (6^3P_1 to 6^1S_0), and a mercury ion line, 194.2 nm ($6^2P_{1/2}$ to $6^2S_{1/2}$), are shown. The insets are the magnified view for the first 500 ns. As can be seen in the trace in the upper-right plot in Figure 4.6, two optical pulses are observed for 185.0 nm emission corresponding to two voltage pulses, which shows that the emission for 185.0 nm is mainly caused by electron impact excitation. On the other hand, the emission of 194.2 nm shows a different behavior in the bottom-left plot. A

slow rise occurs starting from the first voltage pulse and there is an optical pulse at the second current peak. This result shows that mercury ions are produced from the first current peak and the ions are excited by electron impact excitation during the second current peak resulting in the 194.2 nm optical pulse. The slow rise of 194.2 nm from the first current pulse lasts for 1 μs, and then decays for several μs. Considering that the radiative decay time (τ_{ij}) of the transition is 1 ns, this result implies that a slow decaying species is involved in the kinetics of 194.2 nm emission. The slow rise and decay of the waveform of 194.2 nm emission can be explained by the excitation transfer by helium molecular metastable. The helium molecular metastable has a long radiative lifetime reaching several seconds [41], [51] although the non-radiative quenching could be faster in the high pressure and small dimension regime. The contribution by several reactions to populate the Hg $6^2P_{1/2}$ state in the kinetic model can be found in Figure 4.7. The electronic excitation from the mercury ion ground state which is indicated by a blue line shows pulsed behavior when the two current pulses occur. The penning ionization process dominates the production rate of the Hg $6^2P_{1/2}$ state. Subsequent quenching from the highly excited states of mercury ion is also considered. In the He-Hg+ laser system that lases at 614.95 nm, the population inversion is achieved by the charge transfer of helium ion to the Hg $7^2P_{3/2}$ state. The contribution of subsequent quenching from this state to the Hg $6^2P_{1/2}$ state is shown as a red line in Figure 4.7, which is negligible.

The discrepancy between experiment and simulation can be seen in the waveforms of 194.2 nm and 253.7 nm. The decay time of 194.2 nm is larger and the rising of the 253.7 nm in the tail of the waveform is also underestimated in the simulation. For this apparent reason, the limitation comes from the zero-dimensional characteristic of the simulation. The accuracy of the simulation is also limited by the loss mechanism of the mercury ion and electron in the afterglow. In Figure 4.8, the temporal evolution of charged species and the dominant electron loss mechanism can be seen in the plots. The helium dimer ion is the dominant species in the early phase of the afterglow. It is produced by dimerization of helium ion and penning ionization of helium atomic/molecular excited species and recombine with an electron by collisional radiative recombination. In the late phase of the afterglow, the mercury ion becomes dominant to maintain the quasineutrality. Collisional radiative recombination and ambipolar diffusion to the wall are the

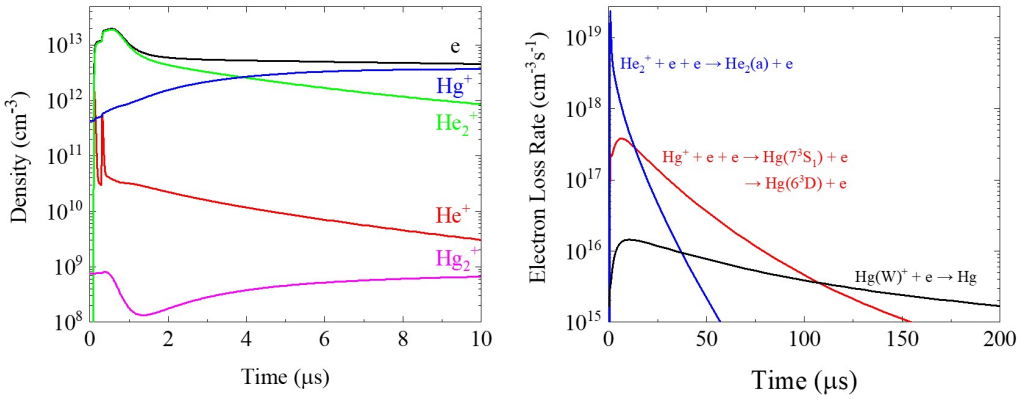

Figure 4.8: (left) Temporal evolution of charged species in the kinetic model, which shows that helium dimer ion is dominant in the early phase of the afterglow while mercury ion is dominant in the late phase the for charge neutrality. (right) Electron loss mechanisms in the extended time in the afterglow. Collisional-radiative recombination and ambipolar diffusion are dominant loss mechanisms of the electrons in the kinetic model.

two important main loss mechanisms of electrons. Since these are strong functions of electron temperature, the quenching rate of the electron temperature is very important. In the elevated electron temperature, the rate for the ambipolar diffusion becomes faster while the dielectronic recombination is not favored as it is proportional to $T_e^{-4.2}$. In the current kinetic model, the energy of the thermal electrons generated by penning ionization or heavy particle collision in the afterglow is not considered. As a result, the electron temperature in the simulation decays rapidly right after the voltage pulse ceases. Second, the rate constants for the volume recombination of the mercury ion and electron are not available. The same rate constant for Cs^+ recombination is implemented in this model as recommended in [52] although they mentioned that the value might not be accurate in low temperatures. In typical cases for mercury discharge, the volume recombination of mercury ion does not have to be included in the kinetic model. In the low pressure regime, it can be assumed that the recombination only occurs at the wall due to the large value of the ambipolar diffusion coefficient. At high pressure and high temperature such as arc discharge, a mercury ion is quickly converted to a molecular ion so the dissociative recombination is dominant. In this work, the operation in high pressure and low temperature could be a special case in which the volume recombination of the atomic mercury ion cannot

be ignored.

The rising tail of 253.7 nm in the afterglow can also be related to the recombination of the mercury ion because the successive quenching from the upper state of mercury neutrals and ions explain the slow rising/plateau in the tail. Thus, reliable information about mercury ion recombination in the volume or at the wall will provide a more precise model.

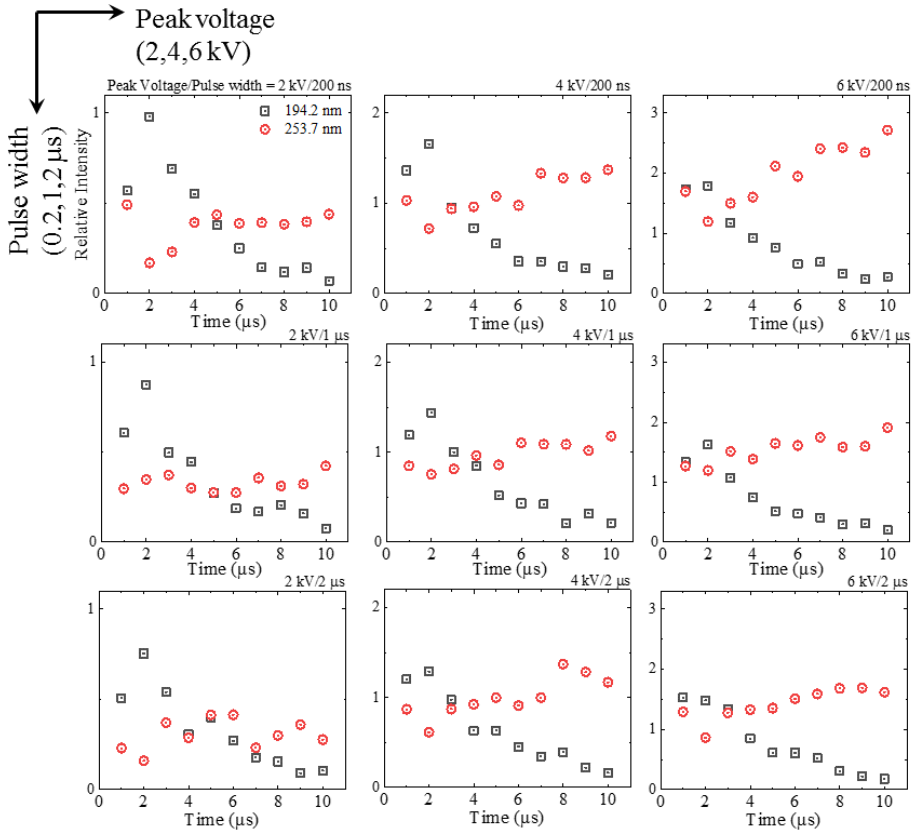

Figure 4.9: A temporally resolved spectrum of 194.2 nm and 253.7 nm varying driving voltages and pulse widths. The PRF is 100 Hz. The relative intensity tends to increase when the peak voltage increases while a larger pulse width leads to lower peak voltage. Note that the relative intensity is rescaled to a larger value as the peak voltage increases (from left to right).

The dependence on the amplitude and the pulse width of the voltage is shown in Figure 4.9. The peak voltage varies as 2, 4, and 6 kV while the pulse width changes as 0.2, 1, and 2 s. Note that the scale of the relative intensity increases as the peak voltage increases. With the same pulse width, the peak value of the 194.2 nm is shown to increase as the peak voltage rises. The dependence of the pulse width is not significant in the case of 194.2 nm.

4.3.1 AC, RF, and Pulsed Power

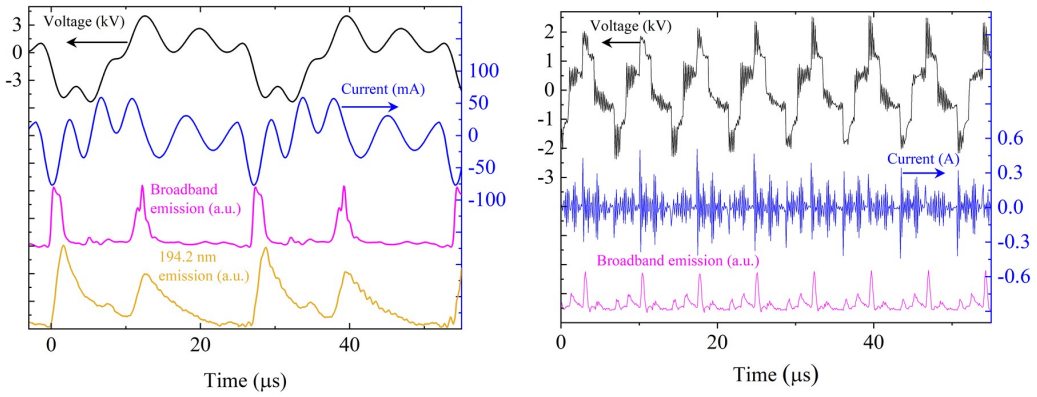

Figure 4.10: (left) The voltage-current-emission waveform when the lamp is driven with an AC module. The driving frequency is 34 kHz. Two optical pulses are observed in the emission waveform. Note that the decay time is larger for the waveform of 194.2 nm emission compared to the broadband emission. (right) The voltage-current-emission waveform when the lamp is driven with a bipolar pulse generator. The driving frequency is 137 kHz.

Different types of power supplies have been tried for more efficient generation of the lamp emission. In Figure 4.10, the V-I waveform as well as the emission waveform are shown when the lamp is driven with an AC module and a bipolar pulse generator. These two power supplies are customized in Eden Park Illumination for the purpose of efficient generation of the excimer lamp. For measurement of the emission waveform of broadband emission, a photosensor amplifier (C6386-01, Hamamatsu) was used. It has the spectral response over 400-1100 nm. The GaP detector (PDA25K2, Thorlab) and a narrowband optical filter for a 193 nm ArF laser are utilized to measure the waveform of 194.2 nm. The FWHM of the optical filter is ≈20 nm, which practically blocks the most of the intensity of other mercury neutral lines such as 185.0 nm and 253.7 nm adjacent to the 194.2 nm line. The peak-to-peak voltage of the AC module is 7 kV and the driving frequency is 37 kHz. Two main emission peaks can be observed for both broadband and 194.2 nm emission waveforms. As already discussed above, the decay time of 194.2 nm is larger compared to the broadband emission due to the long lifetime of the helium molecular metastable. The long tail of the 194.2 nm waveform increases the duty cycle of the lamp emission.

The waveforms taken with a bipolar pulse generator is shown on the right

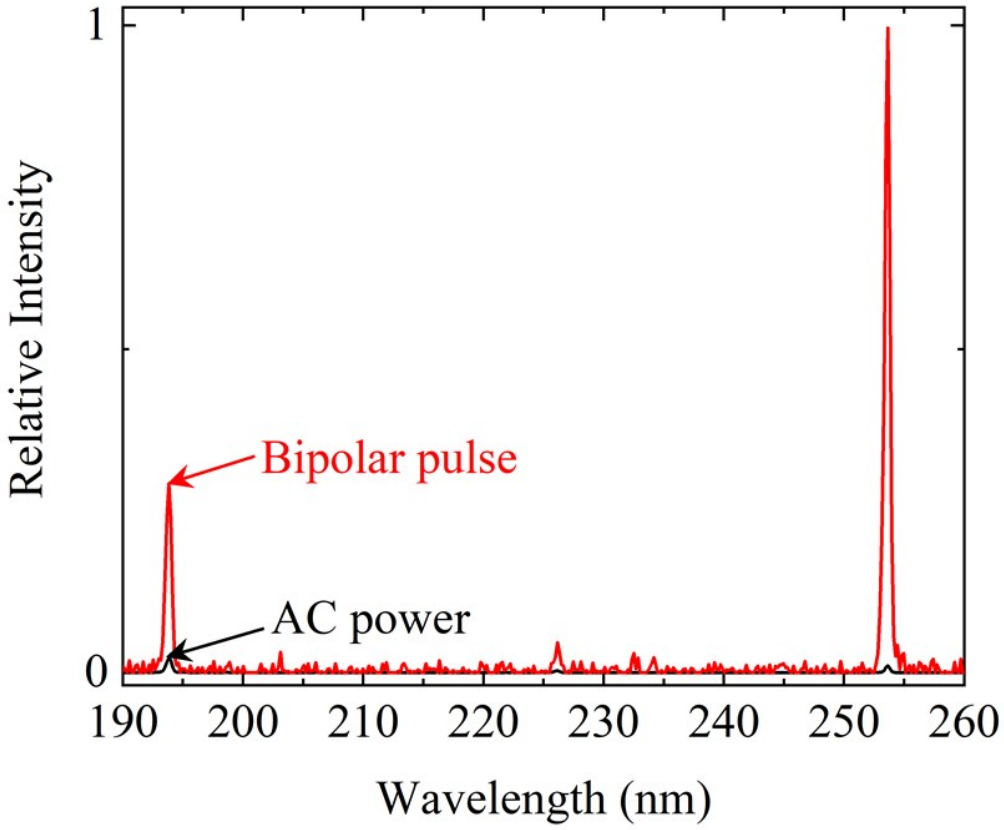

Figure 4.11: A comparison of the spectrum taken with the AC power module and the bipolar pulse generator.

plot in Figure 4.10. The amplitude of each pulse is 1.7 kV and the PRF is 137 kHz. Because of the charge accumulation of DBD, there are two optical pulses in each unipolar pulse resulting in four pulses in total in one cycle of bipolar pulses as shown in the broadband waveform. A comparison of the output spectrum with different power supplies is shown in Figure 4.11. Even with the consideration that the PRF of the bipolar pulse (137 kHz) is larger than the driving frequency of the AC module (34 kHz), the lamp emission is more efficient with the bipolar pulsed operation. A pulse operation, especially with fast rise time and a shorter pulse width, is known to shift the electron energy distribution function (EEDF) to higher energy which results in a larger ionization degree and excitation of highly excited state [24]. For example, the pulsed operation of plasma discharge has shown to produce high electron density up to 10^{17} cm^{-3} [26]. The efficient generation of excimer emission has also been achieved with a fast pulse operation.

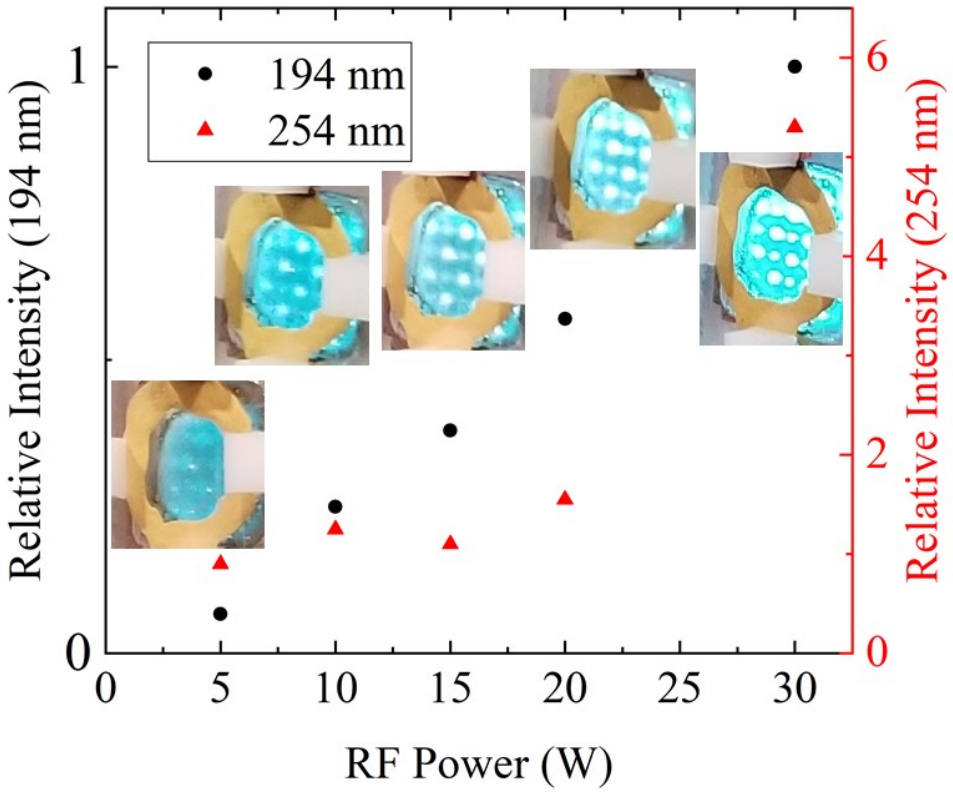

Figure 4.12: Relative intensities of 194.2 nm and 253.7 nm emission when the lamp is driven with RF power. The photo shows the discharge image of the lamp for different RF power.

The lamp is also driven with a 13.56 MHz RF power supply. In Figure 4.12, the relative intensities of 194.2 nm and 253.7 nm versus RF power are shown with the discharge image. The RF power supply (RFG, Barthel) is equipped with an impedance matching box. The RF operation has several advantages upon AC or pulsed operation. The duty cycle of the lamp becomes 100%. Also, it may experience less negative effect due to sputtering of heavy mercury ions. The detailed discussion about sputtering of heavy mercury ions will be held in a later section. However, it was measured that the output power of 194.2 nm is comparable to the AC module when the RF power is 15 W. Thus, RF power is not optimized for efficient generation of 194.2 nm.

4.3.2 Temperature Dependence

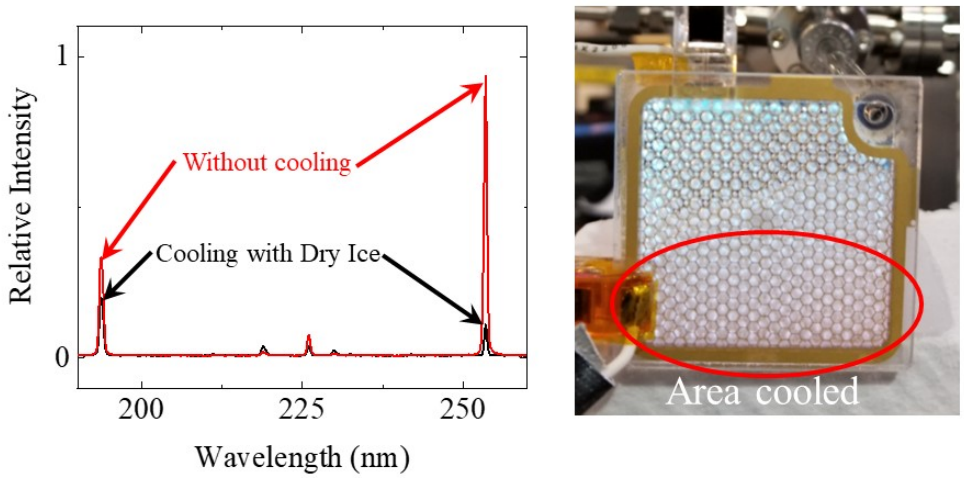

Figure 4.13: (left) A spectrum showing the temperature dependence of the ratio of 194.2 nm and 254.7 nm. (right) A lamp with a size of 50 mm by 50 mm is partially cooled by dry ice. The cooled area is indicated by the red circle. The visible color changes as the helium lines dominate due to a decrease in mercury vapor number density.

The effect of the temperature for a ratio of 194.2 nm to 253.7 nm is shown in Figure 4.13. The relative intensity of 253.7 nm to 194.2 nm is important because the PMT used in the mercury ion clock has a sensitivity in 253.7 nm. Even though an optical filter is placed, the 253.7 nm line still acts as noise to the PMT. Thus, lowering the intensity of 253.7 nm enhances the performance of the ion clock.

For the experiment, a lamp with a size of 50 mm by 50 mm is used. The lamp is driven with a 37 kHz AC module and the bottom half is cooled with dry ice as marked by red circle in the photo at the right in Figure 4.13. As the gas temperature decreases, the helium emission lines dominate as visually seen as light purple in the photo at the bottom while the upper half is dominant by mercury discharge emission showing blue-green color. The spectrum in Figure 4.13 shows that 253.7 nm has a strong dependence on the temperature while the 194.2 nm has less dependence. This is because the excitation mechanism is different. The 194.2 nm emission is governed mostly by the number of helium molecular metastables while the intensity of the 253.7 nm is excited by direct electron impact excitation. A larger number

density of mercury vapor means there are more excited states of mercury followed by the Maxwell-Boltzmann distribution in thermal equilibrium. In contrast, as penning ionization by excimer collision is the main mechanism to excite the upper state of 194.2 nm, the population of the $6^2P_{1/2}$ is limited by the number density of helium molecular metastables. The mercury vapor pressure is a function of temperature, but the effect of gas temperature to the number density of helium excited species is less significant. For example, the mercury number density is 9×10^{13} cm^{-3} in 300 K. When the gas temperature is 400 K, the density increases to 3×10^{16} cm^{-3}. The average number density of helium molecular metastable in the kinetic model is approximately 10^{12} cm^{-3} which is comparable to the average electron density. Although the destruction frequency of helium molecular metastable changes as the gas temperature changes, it is less significant compared to the change in the mercury number density.

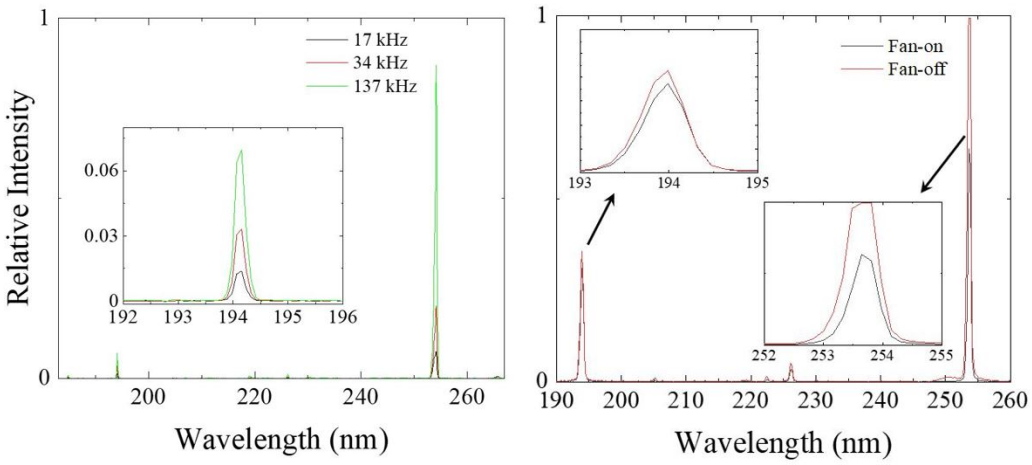

Figure 4.14: (left) UV/VUV spectrum with different driving frequency of a bipolar power supply. (right) UV/VUV spectrum with and without fan-cooling. The driving frequency is 137 kHz.

The temperature change can also be observed in a bipolar pulsed operation. The spectrum on the left in Figure 4.14 shows the intensity change in different PRF of the bipolar pulse. The surface temperature of the window was measured by an IR camera. At the maximum frequency of 137 kHz, the surface temperature exceeds 120 °C by Joule heating of the gas and displacement current in dielectric materials. The result is a strong 254 nm radiation at higher PRF. The ratio of 194.2 nm and 253.7 nm is 0.19 at 17 kHz, but it

decreases to 0.08 at 137 kHz. However, with cooling by a fan, the ratio can be increased significantly while the absolute intensity of 194.2 nm maintains, which is shown in the right spectrum in Figure 4.14. The surface temperature with fan-cooling is 75 °C. The 194.2 nm intensity remains almost constant while the 253.7 nm intensity is decreased to the point that it is comparable to the intensity of 194.2 nm.

4.3.3 Pressure Dependence

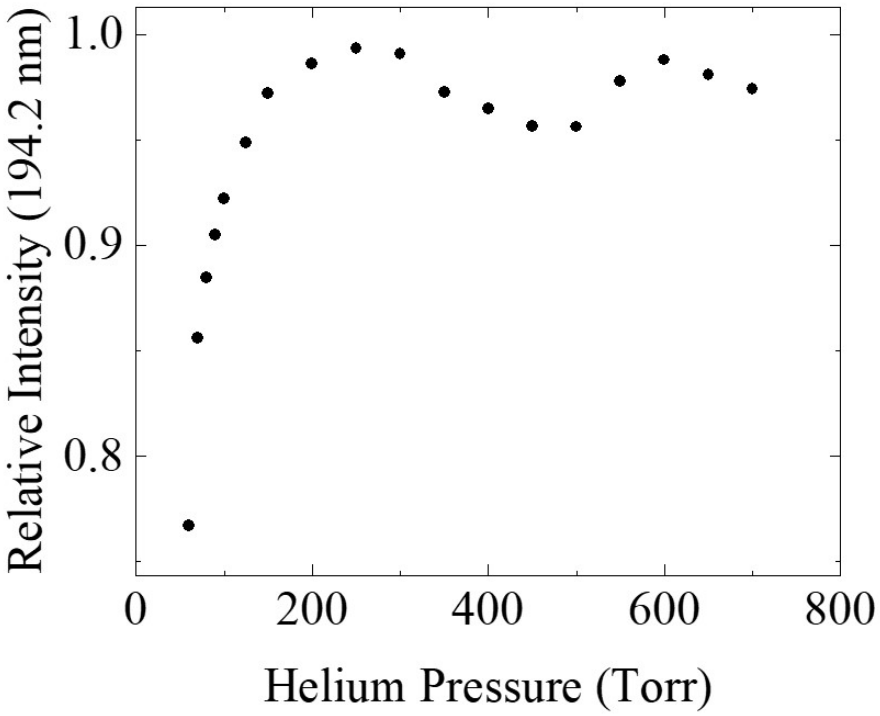

Figure 4.15: The relative intensity of 194.2 nm while the lamp is loaded to a vacuum chamber. Helium flow was slowly fed to the lamp. The plot shows that the intensity of 194.2 nm is reduced at low pressure.

Helium buffer gas pressure is an important parameter for the lamp performance since the excimer formation is a three-body process which is more favored in high pressure. In Figure 4.15, the relative intensity of 194.2 nm was measured while helium was being fed slowly to the lamp through the gas feed line that is loaded to a vacuum chamber. At pressure from 200 Torr

to 760 Torr, the intensity is relatively constant. However, at pressures lower than 200 Torr, it shows a rapid drop.

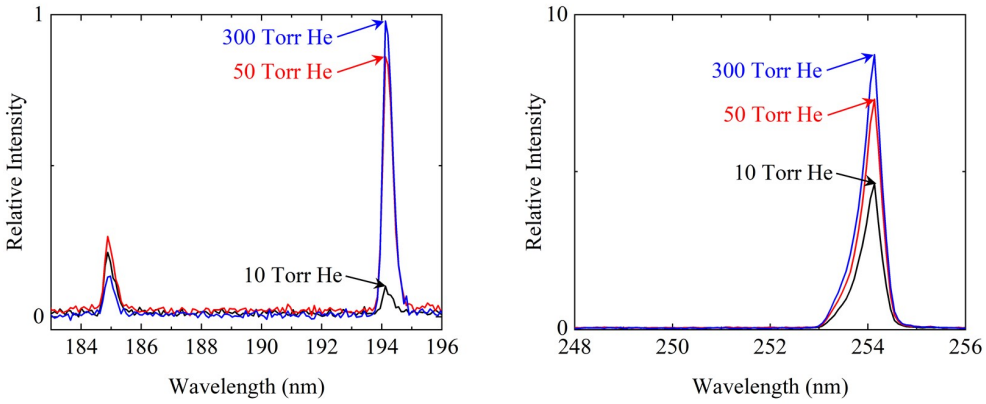

Figure 4.16: A spectrum shows the relative intensities of three mercury emission lines that depend on the helium buffer gas pressure. The lamps were sealed off after they are filled with helium buffer gas with different pressure. The highest pressure, 300 Torr, has shown the largest intensity of 194.2 nm.

Although the result in Figure 4.15 reveals the general tendency of pressure dependence, experimental artifacts may be introduced since the measurement was performed while the lamp was loaded to the vacuum chamber. For instance, mercury vapor number density in the discharge volume might not be in the steady state while the helium gas is being fed through the gas feeding line. Thus, a more precise measurement of the spectrum in different pressures has been performed as shown in Figure 4.16. In this case, each lamp is filled with the desired pressure and the gas feeding line is sealed off. The result confirms that the higher pressure is more preferable to increase the intensity of 194.2 nm. The two mercury atomic lines, 185.0 nm and 253.7 nm, show relatively weaker dependence in pressure compared to the mercury ion line. The main mechanism to populate the excited state of neutral atoms is direct impact excitation. The population of these states is governed by the electron energy distribution and absolute number density of electrons and mercury neutrals while the mercury ion states are populated largely by the number density of helium molecular metastable as discussed above.

4.3.4 Operation in Ne

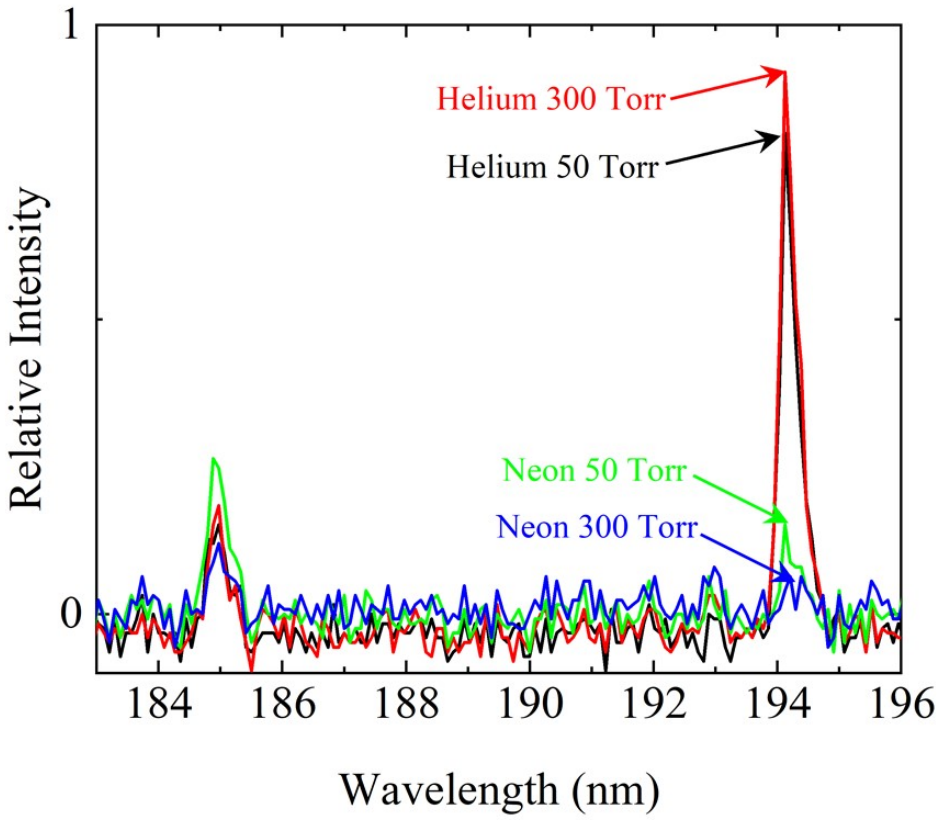

Figure 4.17: A spectrum showing that the generation of 194.2 nm is more efficient with helium buffer gas compared to neon.

The lowest excited states of Ne lie at 16.6-16.9 eV which may be resonant with the $6^2P_{1/2}$ state of Hg^+. Figure 4.17 shows the spectrum of lamps with different buffer gas and pressure. As already discussed above, the higher pressure of helium buffer gas shows a stronger intensity in 194.2 nm. In the case of neon, the intensity of the lamp is weaker compared to the helium buffer gas. Also, lower pressure showed less intensity in 194.2 nm emission. This may be caused by the lower number density of the atomic excited state of neon because the atomic excited states are quickly converted to the molecular excited state in a highly colliding environment. Thus, the number density of atomic excited species is less in high pressure. However, a detailed analysis is required for the kinetic of the Ne-Hg system as the electron density, the EEDF and neon molecular metastable may play a role in excitation of the

$Hg^+(6^2P_{1/2})$. Argon has also been tried by the author, but it shows negligible emission in 194.2 nm.

4.4 Lifetime

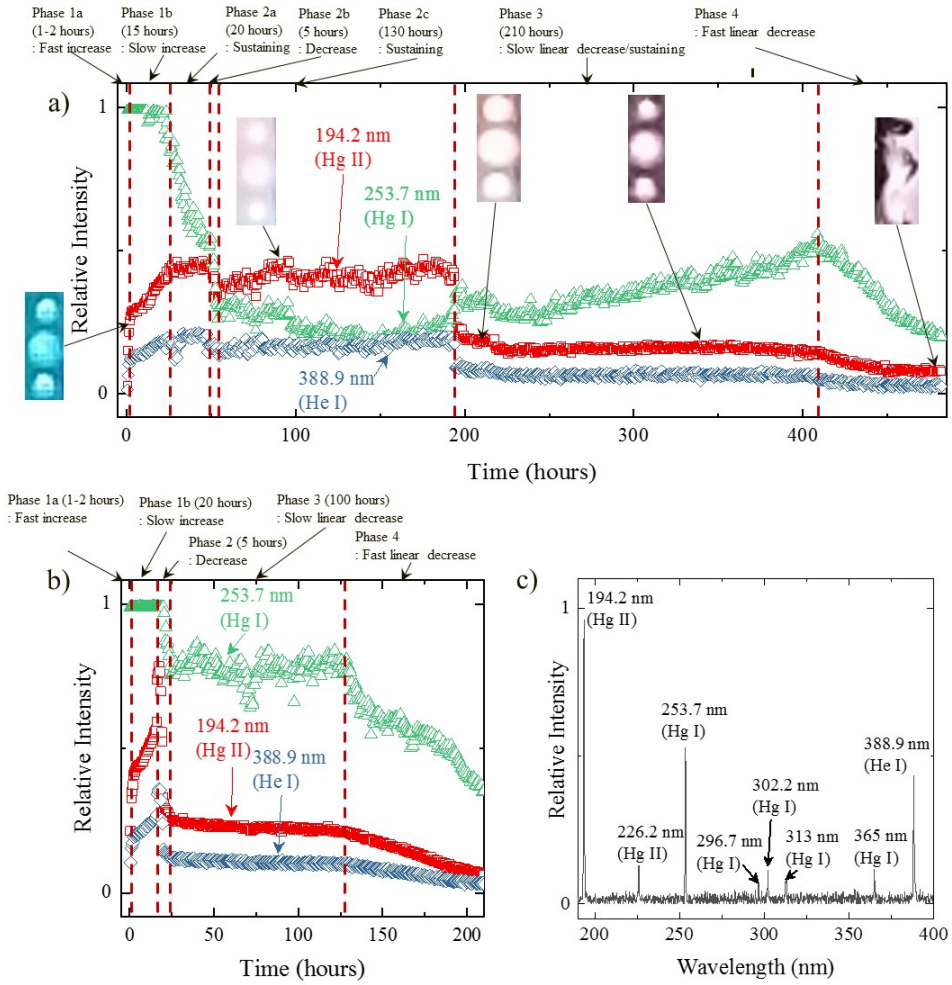

Figure 4.18: A plot showing the relative intensities of three different lines emitted by the lamp. The lamp is coated with alumina with a thickness of 100 nm. The pressure of the helium gas is 600 Torr.

As helium is utilized as a buffer gas in the current work, a permeation rate through the lamp body also has to be considered. Figure 4.18 is the lifetime test result for lamps filled with two different pressures of helium buffer gas which are 600 Torr (top) and 300 Torr (bottom-left). A compact

spectrometer (SPM, Photon Control) is used to trace the spectrum of the lamp. The data points were taken every 30 min.

The example of the spectrum taken at 150 hours after the discharge begins is shown at the bottom-right in Figure 4.18. The discharge phases can be divided largely by four segments based on the intensity of 194.2 nm and the visual discharge mode. The phase change can be explained mainly by the helium leakage of the lamp and the blackening of the window. Three cavities are shown in the plot as insets. The arrow indicates the time when the photo was taken. In the first phase which lasts around 15-20 hours, the lamp intensity slowly increases. The phase is so-called an aging phase. After the aging process is done, the mercury vapor density in discharge volume decreases which can be indicated by the intensity drop in 253.7 nm. The mercury number density drop can be explained by the transport of mercury vapor to the cold spot of the lamp body due to the temperature gradient. The coldest spot of the lamp body is the gas feeding line. The tiny size of mercury droplets was observed moved outward from the discharge volume toward the tip of the gas feeding line in the long time scale.

After the system reaches the equilibrium, a diffusive mode is observed for the lamp filled with 600 Torr of He. The mode change can be seen visually since the dominant color is produced by helium lines which is bright pink and the discharge fills the whole gap between the electrodes while it was confined in the cavity in the beginning. Since the main pumping mechanism of 194.2 nm emission is excitation transfer by helium excimer, strong helium lines could be an indication of efficient generation of 194.2 nm. As a result, the intensity of 194.2 nm is strongest in this phase and the ratio of 194.2 nm to 253.7 nm is the largest. It should be noted that this discharge mode is not seen with the lamp filled with 300 Torr of He. After 130 hours of operation of the discharge mode, another mode change was observed. The discharge is again constricted to the cavities. The relative intensity of 194.2 nm drops and the intensity of 253.7 nm increases. A slow increase in 253.7 nm of the lamp filled with 600 Torr of helium is due to the discharge in the gas filling tube. As the helium gas pressure drops, a discharge occurs and the intensity becomes stronger in the gas filling tube as the tip of the tube acts as a floating ground. This could be another indication of helium leakage. As the pressure drops, *pd* value decreases, which changes the discharge voltage in the Paschen curve.

Phase 3 has been observed for both cases (300 Torr of helium and 600 Torr of helium). In this stage, the darkening of the window and the cavities is visually observed. After 200 hours of operation in this discharge mode, the darkening of the window becomes significant resulting in the drops in the intensity of any VUV-UV lines. From the observation, it can be concluded that the darkening occurs mainly at a low pressure of helium. The bombardment of energetic mercury ions may play an important role in blackening. The dense helium neutrals take away the kinetic energy from the mercury ion in the collisional sheath before it hits the wall. But as the helium pressure drops, the kinetic energy of mercury ions becomes more significant when they hit the wall. Moreover, a set of experiments that were performed with lamps filled with low pressure between 10-50 Torr showed that darkening occurred only within 10-20 hours of operation.

In conclusion, in the pressure range between 10-760 Torr, higher pressure of helium has shown better performance in terms of the intensity and the lifetime of the lamp as excimer formation by dimerization is preferred and blackening of the window is less significant at high pressure.

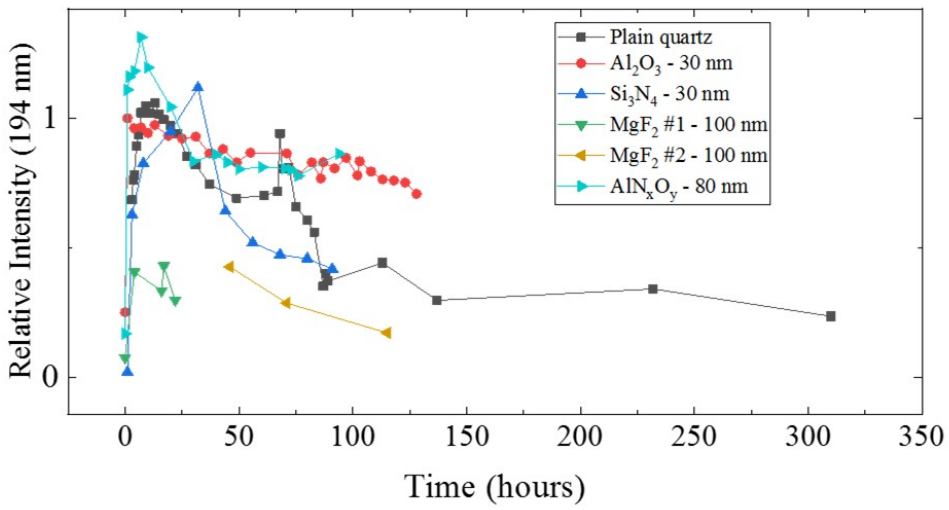

Figure 4.19: A plot showing the lifetime of lamps with different coating materials.

The lifetime test has also been done with different coating materials. Figure 4.19. shows the 194.2 nm intensity changes for different coating materials. The black dot is done with a lamp without any coating which is indicated as plain quartz. The best performance is observed with alumina or AlN_xO_y

coating. The alumina coating is known to suppress darkening of the lamp [53]. All the best performing lamps were coated with alumina. There could be an effect of secondary emission coefficient change as coating materials change since a different discharge mode has been observed with alumina coating. For Si_3N_4 or MgF_2 coating, the window becomes opaque quickly after around 100 hours of operation.

CHAPTER 5

CONCLUSION

New concepts of optical sources in which excimers play important roles are demonstrated. First, a gaseous laser amplifier that exploits atomic interactions between cesium (Cs) and a rare gas (Ar or Xe) is studied. A total optical-to-optical efficiency of 28% with respect to absorbed pump power and a gain broadening of 125 GHz are achieved with a Cs-Ar gas mixture. The medium is photoexcited at 836.7 nm through a free-free molecular transition, $B^2\Sigma^+_{1/2} \leftarrow X^2\Sigma^+_{1/2}$, with a pulse duration of 8 ns. The amplification occurs on the transition near the Cs D_2 line ($6^2P_{3/2} \leftarrow 6^2\ S_{1/2}$) after dissociation of the Cs-Ar thermal pair. The large bandwidths of photoexcitation and gain spectrum are attributed to a Franck-Condon region in the interaction potential curve of Cs and Ar. It is shown that the efficiency can be adjusted by the temperature and spin polarization. Optical amplification on the red satellite of the Cs-Xe atomic pair is observed experimentally, which is possibly attributed to free←free molecular transition. The Franck-Condon calculation is performed to modify the $B^2\Sigma^+_{1/2}$ state potential curve by comparing the simulated spectrum to the experimental one. These unique features allow the alkali-rare gas system to be utilized as a high power IR source and a precise tool for atomic spectroscopy.

Second, the efficient generation of the Hg^+ line ($6^2P_{1/2}\rightarrow 6^2S_{1/2}$) in microplasmas is realized and the unique kinetic pathway is suggested. The collision between a helium metastable molecule ($a^3\Sigma^+_u$) and a neutral mercury atom is responsible for the population of the $Hg^+(6^2P_{1/2})$ and the subsequent radiative transition of 194.2 nm in a plasma state. The kinetic pathway is validated by observing the output intensity of the 194.2 nm emission while the pressure and temperature are varied. A zero-dimensional kinetic simulation also supports the kinetic pathway by comparing the waveform of the output emission to the simulated curve.

In conclusion, the dynamic of the excimers efficiently bridging the input

optical or electrical energy to the output emission of the optical medium has been shown in this work.

APPENDIX A

LIST OF THE RATE CONSTANTS

Helium

Reaction	Rate constant	Reference
Electronic Excitation		
$e + He \leftrightarrow e + He(2^1S)$	Bolsig+ $He \leftrightarrow He(2^1S)$	[54]
$e + He \leftrightarrow e + He(2^3S)$	Bolsig+ $He \leftrightarrow He(2^3S)$	[54]
$e + He \leftrightarrow e + He(2^3P)$	Bolsig+ $He \leftrightarrow He(2^3P)$	[54]
$e + He \leftrightarrow e + He(N)$	Bolsig+ $He \rightarrow He(N)$	[54]
$e + He(2^3S) \leftrightarrow e + He(2^1S)$	Bolsig+ $He(2^3S) \leftrightarrow He(2^1S)$	[55]
$e + He(2^3S) \leftrightarrow e + He(2^3P)$	Bolsig+ $He(2^3S) \leftrightarrow He(2^3P)$	[55]
$e + He(2^3S) \leftrightarrow e + He(N)$	Bolsig+ $He(2^3S) \leftrightarrow He(N)$	[55]
$e + He(2^1S) \leftrightarrow e + He(2^3P)$	Bolsig+ $He(2^1S) \leftrightarrow He(2^3P)$	[55]
$e + He(2^1S) \leftrightarrow e + He(N)$	Bolsig+ $He(2^1S) \leftrightarrow He(N)$	[55]
$e + He(2^3P) \leftrightarrow e + He(N)$	Bolsig+ $He(2^3P) \leftrightarrow He(N)$	[55]
Electronic Ionization		
$e + He \rightarrow e + e + He^+$	Bolsig+ $He \rightarrow He^+$	[54]
$e + He(2^1S) \rightarrow e + e + He^+$	Bolsig+ $He^* \rightarrow He^+$	[54]
$e + He(2^3S) \rightarrow e + e + He^+$	Bolsig+ $He^* \rightarrow He^+$	[54]
$e + He(2^3P) \rightarrow e + e + He^+$	Bolsig+ $He^* \rightarrow He^+$	[54]
$e + He(N) \rightarrow e + e + He^+$	Bolsig+ $He^* \rightarrow He^+$	[54]
Ion Recombination		
$e + e + He^+ \rightarrow e + He(2^1S)$	$0.06 \times 6 \times 10^{-20} \times (T_e/T_g)^{-4}$	[56], [57]
$e + e + He^+ \rightarrow e + He(2^3S)$	$0.19 \times 6 \times 10^{-20} \times (T_e/T_g)^{-4}$	[56], [57]
$e + e + He^+ \rightarrow e + He(2^3P)$	$0.56 \times 6 \times 10^{-20} \times (T_e/T_g)^{-4}$	[56], [57]
$e + e + He^+ \rightarrow e + He(N)$	$0.19 \times 6 \times 10^{-20} \times (T_e/T_g)^{-4}$	[56], [57]
$e + He_2^+ \rightarrow He(2^1S) + He$	$0.06 \times 8.9 \times 10^{-9} \times (T_e/T_g)^{-1.5}$	[58]
$e + He_2^+ \rightarrow He(2^3S) + He$	$0.56 \times 8.9 \times 10^{-9} \times (T_e/T_g)^{-1.5}$	[58]
$e + He_2^+ \rightarrow He(2^3P) + He$	$0.19 \times 8.9 \times 10^{-9} \times (T_e/T_g)^{-1.5}$	[58]

$e + He_2^+ \rightarrow He(N) + He$	$0.19 \times 8.9 \times 10^{-9} \times (T_e/T_g)^{-1.5}$	[58]
$e + e + He_2^+$		
$\rightarrow e + He_2(a^3\Sigma_u^+)$	$0.75 \times 4 \times 10^{-20} \times (T_e/T_g)^{-4}$	[56]
$e + e + He_2^+$		
$\rightarrow e + He_2(A^1\Sigma_u^+)$	$0.25 \times 4 \times 10^{-20} \times (T_e/T_g)^{-4}$	[56]
$e + He + He_2^+$		
$\rightarrow He + He(2^3P)$	$0.75 \times 1.1 \times 10^{-27} \times (T_e/T_g)^{-2}$	[59], [57]
Heavy Particle Collision		
$He + He + He(2^3S)$		
$\rightarrow He + He_2(a^3\Sigma_u^+)$	$8.1 \times 10^{-36} \times T_g \times exp(-650/T_g)$	[60]
$He + He + He(2^1S)$		
$\rightarrow He + He_2(A^1\Sigma_u^+)$	1.3×10^{-33}	[57]
$He + He + He(2^3P)$		
$\rightarrow He + He_2(a^3\Sigma_u^+)$	1.6×10^{-32}	[57]
$He + He + He^+$		
$\rightarrow He + He_2^+$	$1.4 \times 10^{-31} \times (T_g/300)^{-0.6}$	[55]
$He + He(N) \rightarrow e + He_2^+$	1.5×10^{-11}	[58]
$He^* + He^* \rightarrow e + He_2^+$	$0.7 \times 2.9 \times 10^{-9} \times (T_g/300)^{0.5}$	[55], [56]
$He^* + He^* \rightarrow e + He + He^+$	$0.3 \times 2.9 \times 10^{-9} \times (T_g/300)^{0.5}$	[55], [56]
$He^* + He_2(a^3\Sigma_u^+)$		
$\rightarrow e + He + He_2^+$	$0.7 \times 2.9 \times 10^{-9} \times (T_g/300)^{0.5}$	[55], [56]
$He^* + He_2(a^3\Sigma_u^+)$		
$\rightarrow e + He + He + He^+$	$0.3 \times 2.9 \times 10^{-9} \times (T_g/300)^{0.5}$	[55], [56]
$He_2(a^3\Sigma_u^+) + He_2(a^3\Sigma_u^+)$		
$\rightarrow e + He + He + He_2^+$	$0.7 \times 1.5 \times 10^{-9}$	[56]
$He_2(a^3\Sigma_u^+) + He_2(a^3\Sigma_u^+)$		
$\rightarrow e + He + He + He + He^+$	$0.3 \times 1.5 \times 10^{-9}$	[56]
$e + He_2(a^3\Sigma_u^+)$		
$\rightarrow e + e + He_2^+$	$9.75 \times 10^{-10} \times (T_e/11600)^{0.71} \times exp(-3.4 \times 11600/T_e)$	[61]
$e + He_2(a^3\Sigma_u^+)$		
$\rightarrow e + He + He$	3.8×10^{-9}	[56]
$He + He_2(a^3\Sigma_u^+)$		
$\rightarrow He + He + He$	4.9×10^{-16}	[62]
Spontaenous Emission		
$He_2(A^1\Sigma_u^+)$		

$\rightarrow$ He + He + $h\nu$($\sim$75 nm)	1.8×10^9	[63]
$He(2^3P)$		
$\rightarrow$ $He(2^3S)$+$h\nu$(1083 nm)	1.0216×10^7	[63]
$He(N) \rightarrow He(2^1S)+h\nu$	1×10^7	Estimated
$He(N) \rightarrow He(2^3S)+h\nu$	1×10^7	Estimated
$He(N) \rightarrow He(2^3P)+h\nu$	1×10^7	Estimated

Mercury

Reaction	Rate constant	Reference
Electronic Excitation		
$e + Hg \leftrightarrow e + Hg(6^3P_0)$	Bolsig+ $Hg \leftrightarrow Hg(6^3P_0)$	[54]
$e + Hg \leftrightarrow e + Hg(6^3P_1)$	Bolsig+ $Hg \leftrightarrow Hg(6^3P_1)$	[54]
$e + Hg \leftrightarrow e + Hg(6^3P_2)$	Bolsig+ $Hg \leftrightarrow Hg(6^3P_2)$	[54]
$e + Hg \leftrightarrow e + Hg(7^3S_1)$	Bolsig+ $Hg \leftrightarrow Hg(7^3S_1)$	[54]
$e + Hg \leftrightarrow e + Hg(6^3D)$	Bolsig+ $Hg \leftrightarrow Hg(7^3S_1)$	[54]
$e+Hg(6^3P_0) \leftrightarrow e+Hg(6^3P_1)$	Bolsig+ $Hg(6^3P_1) \leftrightarrow Hg(6^3P_2)$	[64]
$e+Hg(6^3P_0) \leftrightarrow e+Hg(6^3P_2)$	Bolsig+ $Hg(6^3P_1) \leftrightarrow Hg(6^3P_2)$	[64]
$e+Hg(6^3P_0) \leftrightarrow e+Hg(6^1P_1)$	Bolsig+ $Hg(6^3P_0) \leftrightarrow Hg(7^3S_1)$	[64]
$e+Hg(6^3P_0) \leftrightarrow e+Hg(7^3S_1)$	Bolsig+ $Hg(6^3P_0) \leftrightarrow Hg(7^3S_1)$	[64]
$e+Hg(6^3P_0) \leftrightarrow e+Hg(6^3D)$	Bolsig+ $Hg(6^3P_0) \leftrightarrow Hg(7^3S_1)$	[64]
$e+Hg(6^3P_1) \leftrightarrow e+Hg(6^3P_2)$	Bolsig+ $Hg(6^1P_0) \leftrightarrow Hg(6^3P_2)$	[64]
$e+Hg(6^3P_1) \leftrightarrow e+Hg(6^1P_1)$	Bolsig+ $Hg(6^3P_0) \leftrightarrow Hg(7^3S_1)$	[64]
$e+Hg(6^3P_1) \leftrightarrow e+Hg(7^3S_1)$	Bolsig+ $Hg(6^3P_0) \leftrightarrow Hg(7^3S_1)$	[64]
$e+Hg(6^3P_1) \leftrightarrow e+Hg(6^3D)$	Bolsig+ $Hg(6^3P_0) \leftrightarrow Hg(7^3S_1)$	[64]
$e+Hg(6^3P_2) \leftrightarrow e+Hg(6^1P_1)$	Bolsig+ $Hg(6^3P_0) \leftrightarrow Hg(7^3S_1)$	[64]
$e+Hg(6^3P_2) \leftrightarrow e+Hg(7^3S_1)$	Bolsig+ $Hg(6^3P_0) \leftrightarrow Hg(7^3S_1)$	[64]
$e+Hg(6^3P_2) \leftrightarrow e+Hg(6^3D)$	Bolsig+ $Hg(6^3P_0) \leftrightarrow Hg(7^3S_1)$	[64]
$e+Hg^+ \leftrightarrow e+Hg^+(6^2P_{1/2})$	Bolsig+ $Hg^+ \leftrightarrow Hg^+(6^2P_{1/2})$	[65]
$e+Hg^+ \leftrightarrow e+Hg^+(6^2P_{3/2})$	Bolsig+ $Hg^+ \leftrightarrow Hg^+(6^2P_{3/2})$	[65]
Electronic Ionization		
$e+Hg \rightarrow e+e+Hg^+$	Bolsig+ $Hg \rightarrow Hg^+$	[54]
$e+Hg(6^3P_0) \rightarrow e+e+Hg^+$	Bolsig+ $Hg(6^3P) \rightarrow Hg^+$	[66]
$e+Hg(6^3P_1) \rightarrow e+e+Hg^+$	Bolsig+ $Hg(6^3P) \rightarrow Hg^+$	[66]
$e+Hg(6^3P_2) \rightarrow e+e+Hg^+$	Bolsig+ $Hg(6^3P) \rightarrow Hg^+$	[66]

$e+Hg(6^1P_1) \rightarrow e+e+Hg^+$	Bolsig+ $Hg(7^3S_1) \rightarrow Hg^+$	[66]
$e+Hg(7^3S_1) \rightarrow e+e+Hg^+$	Bolsig+ $Hg(7^3S_1) \rightarrow Hg^+$	[66]
$e+Hg(6^3D) \rightarrow e+e+Hg^+$	Bolsig+ $Hg(6^3D) \rightarrow Hg^+$	[66]
Ion Recombination		
$e+e+Hg^+ \rightarrow e+Hg(7^3S_1)$	$0.5 \times 2.4 \times 10^{-10} \times T_e^{-4.2}$	[67], [52]
$e+e+Hg^+ \rightarrow e+Hg(6^3D)$	$0.5 \times 2.4 \times 10^{-10} \times T_e^{-4.2}$	[67], [52]
$e+He+Hg^+$ $\rightarrow He+Hg(7^3S_1)$	$0.5 \times 4 \times 10^{-29} \times (T_e/T_g)^{-2.5}$	[67], [52]
$e+He+Hg^+$ $\rightarrow He+Hg(6^3D)$	$0.5 \times 4 \times 10^{-29} \times (T_e/T_g)^{-2.5}$	[67], [52]
$e+Hg_2^+ \rightarrow Hg+Hg(6^3P_0)$	$0.16 \times 4.2 \times 10^{-7} \times (T_e/T_g)^{-1.1}$	[68]
$e+Hg_2^+ \rightarrow Hg+Hg(6^3P_1)$	$0.16 \times 4.2 \times 10^{-7} \times (T_e/T_g)^{-1.1}$	[68]
$e+Hg_2^+ \rightarrow Hg+Hg(6^3P_2)$	$0.16 \times 4.2 \times 10^{-7} \times (T_e/T_g)^{-1.1}$	[68]
$e+Hg_2^+ \rightarrow Hg+Hg(6^1P_1)$	$0.16 \times 4.2 \times 10^{-7} \times (T_e/T_g)^{-1.1}$	[68]
$e+Hg_2^+ \rightarrow Hg+Hg(7^3S_1)$	$0.16 \times 4.2 \times 10^{-7} \times (T_e/T_g)^{-1.1}$	[68]
$e+Hg_2^+ \rightarrow Hg+Hg(6^3D)$	$0.16 \times 4.2 \times 10^{-7} \times (T_e/T_g)^{-1.1}$	[68]
Heavy Particle Collision		
$He+Hg+Hg^+ \rightarrow He+Hg_2^+$	1.7×10^{-31}	[69]
$Hg^*+Hg^* \rightarrow e+Hg_2^+$	a$\times 3.5 \times 10^{-10}$	[70], [71]
$Hg + He_2(a^3\Sigma_u^+)$ $\rightarrow Hg^+(6^2P_{1/2})+He+He$	$0.5 \times 5 \times 10^{-10}$	[72]
$Hg + He_2(a^3\Sigma_u^+)$ $\rightarrow Hg^+(6^2P_{3/2})+He+He$	$0.5 \times 5 \times 10^{-10}$	[72]
$Hg + He^+$ $\rightarrow Hg^+(7^2P_{3/2})+He+e$	1.1×10^{-10}	[73]
$Hg(6^3P_0) + He(2^3S)$ $\rightarrow Hg^+(7^2P_{3/2})+He+e$	$0.7 \times 1.1 \times 10^{-10}$	[73], [74]
$Hg(6^3P_1) + He(2^3S)$ $\rightarrow Hg^+(7^2P_{3/2})+He+e$	$0.7 \times 1.1 \times 10^{-10}$	[73], [74]
$Hg(6^3P_2) + He(2^3S)$ $\rightarrow Hg^+(7^2P_{3/2})+He+e$	$0.7 \times 1.1 \times 10^{-10}$	[73], [74]
Spontaenous Emission		
$Hg(6^3P_1) \rightarrow Hg$ $+h\nu(254\text{ nm})$	8.40×10^6	[63]
$Hg(6^1P_1) \rightarrow Hg$ $+h\nu(185.0\text{ nm})$	7.46×10^8	[63]

$Hg(7^3S_1) \rightarrow Hg(6^3P_0)$		
$+h\nu(405\text{ nm})$	2.07×10^7	[63]
$Hg(7^3S_1) \rightarrow Hg(6^3P_1)$		
$+h\nu(436\text{ nm})$	5.6×10^7	[63]
$Hg(7^3S_1) \rightarrow Hg(6^3P_2)$		
$+h\nu(546\text{ nm})$	4.9×10^7	[63]
$Hg(6^3D) \rightarrow Hg(6^3P_0)$		
$+h\nu(297\text{ nm})$	4.6×10^7	[63]
$Hg(6^3D) \rightarrow Hg(6^3P_1)$		
$+h\nu(313\text{ nm})$	6.6×10^7	[63]
$Hg(6^3D) \rightarrow Hg(6^3P_2)$		
$+h\nu(366\text{ nm})$	1.29×10^8	[63]
$Hg(6^3D) \rightarrow Hg(6^1P_1)$		
$+h\nu(577\text{ nm})$	2.36×10^7	[63]
$Hg^+(7^2P_{3/2}) \rightarrow Hg^+(7^2S_{1/2})$		
$+h\nu(615\text{ nm})$	6.2×10^7	[63]
$Hg^+(7^2P_{3/2}) \rightarrow Hg^+(7^2S_{1/2})$		
$+h\nu(89.3\text{ nm})$	6.2×10^7	[63]
$Hg^+(7^2S_{1/2}) \rightarrow Hg^+(6^2P_{3/2})$		
$+h\nu(285\text{ nm})$	3.0×10^8	[63]
$Hg^+(7^2S_{1/2}) \rightarrow Hg^+(6^2P_{1/2})$		
$+h\nu(226\text{ nm})$	3.0×10^8	[63]
$Hg^+(6^2P_{3/2}) \rightarrow Hg^+$		
$+h\nu(165\text{ nm})$	1.2×10^9	[63]
$Hg^+(6^2P_{1/2}) \rightarrow Hg^+$		
$+h\nu(194\text{ nm})$	7.5×10^8	[63]

REFERENCES

[1] D. Cvetko, A. Lausi, A. Morgante, F. Tommasini, P. Cortona, and M. Dondi, "A new model for atom–atom potentials," *The Journal of Chemical Physics*, vol. 100, no. 3, pp. 2052–2057, 1994.

[2] K. Tang and J. Toennies, "The van der Waals potentials between all the rare gas atoms from He to Rn," *The Journal of Chemical Physics*, vol. 118, no. 11, pp. 4976–4983, 2003.

[3] M. L. Ginter and R. Battino, "Potential-energy curves for the He_2 molecule," *The Journal of Chemical Physics*, vol. 52, no. 9, pp. 4469–4474, 1970.

[4] K. Jain, C. G. Willson, and B. J. Lin, "Ultrafast deep UV lithography with excimer lasers," *IEEE Electron Device Letters*, vol. 3, no. 3, pp. 53–55, 1982.

[5] W. F. Krupke, R. J. Beach, V. K. Kanz, and S. A. Payne, "Resonance transition 795-nm rubidium laser," *Optics Letters*, vol. 28, no. 23, pp. 2336–2338, 2003.

[6] B. Zhdanov, T. Ehrenreich, and R. Knize, "Highly efficient optically pumped cesium vapor laser," *Optics Communications*, vol. 260, no. 2, pp. 696–698, 2006.

[7] B. Zhdanov, C. Maes, T. Ehrenreich, A. Havko, N. Koval, T. Meeker, B. Worker, B. Flusche, and R. Knize, "Optically pumped potassium laser," *Optics Communications*, vol. 270, no. 2, pp. 353–355, 2007.

[8] J. Zweiback and B. Krupke, "Rubidium and potassium alkali lasers," in *High Energy/Average Power Lasers and Intense Beam Applications III*, vol. 7196. International Society for Optics and Photonics, 2009, p. 71960E.

[9] G. A. Pitz and M. D. Anderson, "Recent advances in optically pumped alkali lasers," *Applied Physics Reviews*, vol. 4, no. 4, p. 041101, 2017.

[10] A. V. Bogachev, S. G. Garanin, A. Dudov, V. Eroshenko, S. M. Kulikov, G. Mikaelian, V. A. Panarin, V. Pautov, A. Rus, and S. A. Sukharev, "Diode-pumped caesium vapour laser with closed-cycle laser-active medium circulation," *Quantum Electronics*, vol. 42, no. 2, p. 95, 2012.

[11] M. Endo, R. Nagaoka, H. Nagaoka, T. Nagai, and F. Wani, "Experimental study of the diode pumped alkali laser (DPAL)," in *High Energy/Average Power Lasers and Intense Beam Applications VII*, vol. 8962. International Society for Optics and Photonics, 2014, p. 896205.

[12] J. Readle, C. Wagner, J. Verdeyen, D. Carroll, and J. Eden, "Lasing in Cs at 894.3nm pumped by the dissociation of CsAr excimers," *Electronics Letters*, vol. 44, pp. 1466–1467, 2008.

[13] U. Kogelschatz, "Excimer lamps: History, discharge physics, and industrial applications," in *Atomic and Molecular Pulsed Lasers V*, vol. 5483. International Society for Optics and Photonics, 2004, pp. 272–286.

[14] S.-J. Park, C. M. Herring, A. E. Mironov, J. H. Cho, and J. G. Eden, "25 W of average power at 172 nm in the vacuum ultraviolet from flat, efficient lamps driven by interlaced arrays of microcavity plasmas," *APL Photonics*, vol. 2, no. 4, p. 041302, 2017.

[15] J. Franck and E. Dymond, "Elementary processes of photochemical reactions," *Transactions of the Faraday Society*, vol. 21, pp. 536–542, February 1926.

[16] E. Condon, "A theory of intensity distribution in band systems," *Physical Review*, vol. 28, no. 6, p. 1182, 1926.

[17] P. W. Atkins, J. De Paula, and J. Keeler, *Atkins' Physical Chemistry*. Oxford University Press, 2018.

[18] J. Tellinghuisen, "The Franck-Condon principle in bound-free transitions," *Photodissociation and Photoionization*, vol. 60, pp. 299–369, 1985.

[19] R. Hedges, D. Drummond, and A. Gallagher, "Extreme-wing line broadening and Cs-inert-gas potentials," *Physical Review A*, vol. 6, no. 4, p. 1519, 1972.

[20] N. Allard and J. Kielkopf, "The effect of neutral nonresonant collisions on atomic spectral lines," *Reviews of Modern Physics*, vol. 54, no. 4, p. 1103, 1982.

[21] K. Becker, K. Schoenbach, and J. G. Eden, "Microplasmas and applications," *Journal of Physics D: Applied Physics*, vol. 39, no. 3, p. R55, 2006.

[22] M. A. Lieberman and A. J. Lichtenberg, *Principles of Plasma Discharges and Materials Processing*. John Wiley & Sons, 2005.

[23] D. Go and A. Venkattraman, "Microscale gas breakdown: Ion-enhanced field emission and the modified Paschens curve," *Journal of Physics D: Applied Physics*, vol. 47, no. 50, p. 503001, 2014.

[24] R. H. Stark and K. H. Schoenbach, "Electron heating in atmospheric pressure glow discharges," *Journal of Applied Physics*, vol. 89, no. 7, pp. 3568–3572, 2001.

[25] M. Moselhy, I. Petzenhauser, K. Frank, and K. H. Schoenbach, "Excimer emission from microhollow cathode argon discharges," *Journal of Physics D: Applied Physics*, vol. 36, no. 23, p. 2922, 2003.

[26] D. Yarmolich, Y. E. Krasik, E. Stambulchik, V. Bernshtam, J. Yoon, B. Herrera, S.-J. Park, and J. Eden, "Self-pulsing 10^4 Acm^{-2} current density discharges in dielectric barrier $\mathrm{Al/Al_2O_3}$ microplasma devices," *Applied Physics Letters*, vol. 94, no. 1, p. 011501, 2009.

[27] A.-V. Phelps, "Absorption studies of helium metastable atoms and molecules," *Physical Review*, vol. 99, no. 4, p. 1307, 1955.

[28] J. Frame, P. John, T. DeTemple, and J. G. Eden, "Continuous-wave emission in the ultraviolet from diatomic excimers in a microdischarge," *Applied Physics Letters*, vol. 72, no. 21, pp. 2634–2636, 1998.

[29] P. Kurunczi, J. Lopez, H. Shah, and K. Becker, "Excimer formation in high-pressure microhollow cathode discharge plasmas in helium initiated by low-energy electron collisions," *International Journal of Mass Spectrometry*, vol. 205, no. 1-3, pp. 277–283, 2001.

[30] J. D. Hewitt, J. D. Readle, and J. G. Eden, "Observation of the continuous transformation of a four level laser into a two level system," *Applied Physics Letters*, vol. 101, no. 7, p. 071102, 2012.

[31] J. Pascale and J. Vandeplanque, "Excited molecular terms of the alkali-rare gas atom pairs," *The Journal of Chemical Physics*, vol. 60, no. 6, pp. 2278–2289, 1974.

[32] L. Blank and D. E. Weeks, "Impact broadening, shifting, and asymmetry of the D_1 and D_2 lines of alkali-metal atoms colliding with noble-gas atoms," *Physical Review A*, vol. 90, no. 2, p. 022510, 2014.

[33] V. Vuletić, V. Sautenkov, C. Zimmermann, and T. Hänsch, "Measurement of cesium resonance line self-broadening and shift with doppler-free selective reflection spectroscopy," *Optics Communications*, vol. 99, no. 3-4, pp. 185–190, 1993.

[34] A. Mironov and J. G. Eden, "Manipulating excited state hyperfine level populations in an atomic laser through electronic spin polarization: Controlling upper laser level degeneracy and small signal gain," *Optics Express*, vol. 25, no. 24, pp. 29 676–29 686, 2017.

[35] J. Dhiflaoui, H. Berriche, and M. Heaven, "Theoretical investigation of RbXe and CsXe excimers including the spin–orbit interaction," *Journal of Physics B: Atomic, Molecular and Optical Physics*, vol. 49, no. 20, p. 205101, 2016.

[36] J. D. Hewitt, "Alkali–rare gas photodissociation lasers: Applications to laser physics and atom-atom interactions," Ph.D. dissertation, University of Illinois at Urbana-Champaign, 2013.

[37] J. W. Cooley, "An improved eigenvalue corrector formula for solving the Schrodinger equation for central fields," *Mathematics of Computation*, vol. 15, no. 76, pp. 363–374, 1961.

[38] R. Jones, J. Schloss, and J. Eden, "Excitation spectra for the photoassociation of Kr–F and Xe–I collision pairs in the ultraviolet (208–258 nm)," *The Journal of Chemical Physics*, vol. 98, no. 6, pp. 4317–4334, 1993.

[39] F. Major and G. Werth, "Magnetic hyperfine spectrum of isolated (199 Hg)$^+$ ions," *Applied Physics*, vol. 15, no. 2, pp. 201–208, 1978.

[40] R. L. Tjoelker, J. D. Prestage, E. A. Burt, P. Chen, Y. J. Chong, S. K. Chung, W. Diener, T. Ely, D. G. Enzer, H. Mojaradi et al., "Mercury ion clock for a NASA technology demonstration mission," *IEEE Transactions on Ultrasonics, Ferroelectrics, and Frequency Control*, vol. 63, no. 7, pp. 1034–1043, 2016.

[41] B. Minaev, "Fine structure and radiative lifetime of the low-lying triplet states of the helium excimer," *Phys. Chem. Chem. Phys.*, vol. 5, pp. 2314–2319, 2003.

[42] S. Neeser, R. Tietz, M. Schulz, and H. Langhoff, "Lifetime of the He_2(e), He_2(d) and He_2(f) states," *Zeitschrift für Physik D Atoms, Molecules and Clusters*, vol. 31, no. 1, pp. 61–65, 1994.

[43] S. Pancheshnyi, B. Eismann, G. Hagelaar, and L. Pitchford, "Computer code ZDPlasKin," *University of Toulouse, LAPLACE, CNRS-UPS-INP, Toulouse, France*, 2008.

[44] P. N. Brown, G. D. Byrne, and A. C. Hindmarsh, "VODE: A variable-coefficient ODE solver," *SIAM Journal on Scientific and Statistical Computing*, vol. 10, no. 5, pp. 1038–1051, 1989.

[45] G. Hagelaar, "Bolsig+ Electron Boltzmann equation solver," 2010.

[46] W. Bell, "Visible laser transitions in Hg^+," *Applied Physics Letters*, vol. 4, no. 2, pp. 34–35, 1964.

[47] T. Holstein, "Imprisonment of resonance radiation in gases. II," *Physical Review*, vol. 83, no. 6, p. 1159, 1951.

[48] E. Bogdanov, A. Kudryavtsev, R. Arslanbekov, and V. Kolobov, "Simulation of pulsed dielectric barrier discharge xenon excimer lamp," *Journal of Physics D: Applied Physics*, vol. 37, no. 21, p. 2987, 2004.

[49] W. S. Kang, J. M. Park, Y. Kim, and S. H. Hong, "Numerical study on influences of barrier arrangements on dielectric barrier discharge characteristics," *IEEE Transactions on Plasma Science*, vol. 31, no. 4, pp. 504–510, 2003.

[50] S. Liu and M. Neiger, "Electrical modelling of homogeneous dielectric barrier discharges under an arbitrary excitation voltage," *Journal of Physics D: Applied Physics*, vol. 36, no. 24, p. 3144, 2003.

[51] C. F. Chabalowski, J. O. Jensen, D. R. Yarkony, and B. H. Lengsfield III, "Theoretical study of the radiative lifetime for the spin-forbidden transition $a^3\Sigma_u^+ \rightarrow X^1\Sigma_g^+$ in He_2," *The Journal of Chemical Physics*, vol. 90, no. 4, pp. 2504–2512, 1989.

[52] L. Biberman, V. S. Vorob'ev, and I. Yakubov, "Kinetics of impact-radiation ionization and recombination," *Soviet Physics Uspekhi*, vol. 15, no. 4, p. 375, 1973.

[53] A. Voronov, "New generation of low pressure mercury lamps for producing ozone," *Ozone: Science and Engineering*, vol. 30, no. 6, pp. 395–397, 2008.

[54] L. C. Pitchford, L. L. Alves, K. Bartschat, S. F. Biagi, M.-C. Bordage, I. Bray, C. E. Brion, M. J. Brunger, L. Campbell, A. Chachereau et al., "LXCat: An open-access, web-based platform for data needed for modeling low temperature plasmas," *Plasma Processes and Polymers*, vol. 14, no. 1-2, p. 1600098, 2017.

[55] L. Alves, G. Gousset, and C. Ferreira, "A collisional-radiative model for microwave discharges in helium at low and intermediate pressures," *Journal of Physics D: Applied Physics*, vol. 25, no. 12, p. 1713, 1992.

[56] R. Deloche, P. Monchicourt, M. Cheret, and F. Lambert, "High-pressure helium afterglow at room temperature," *Physical Review A*, vol. 13, no. 3, p. 1140, 1976.

[57] F. Emmert, H. Angermann, R. Dux, and H. Langhoff, "Reaction kinetics of the He(^{2}P) and the He_2^*(a, v) states in high-density helium," *Journal of Physics D: Applied Physics*, vol. 21, no. 5, p. 667, 1988.

[58] Y. B. Golubovskii, V. Maiorov, J. Behnke, and J. Behnke, "Modelling of the homogeneous barrier discharge in helium at atmospheric pressure," *Journal of Physics D: Applied Physics*, vol. 36, no. 1, p. 39, 2002.

[59] D. Bates, "Rydberg dissociative recombination in a helium afterglow," *Journal of Physics B: Atomic and Molecular Physics*, vol. 17, no. 11, p. 2363, 1984.

[60] A. Köymen, F.-C. Tang, X. Zhao, F. Dunning, and G. Walters, "Multiple activation energies for conversion of He(2^3S) atoms to He^2 ($a^3\Sigma_u^+$) molecules in ternary collisions," *Chemical Physics Letters*, vol. 168, no. 5, pp. 405–409, 1990.

[61] S. Rauf and M. J. Kushner, "Dynamics of a coplanar-electrode plasma display panel cell. I. Basic operation," *Journal of Applied Physics*, vol. 85, no. 7, pp. 3460–3469, 1999.

[62] T. Martens, A. Bogaerts, W. Brok, and J. van Dijk, "Computer simulations of a dielectric barrier discharge used for analytical spectrometry," *Analytical and Bioanalytical Chemistry*, vol. 388, no. 8, pp. 1583–1594, 2007.

[63] Y. Ralchenko, A. Kramida, J. Reader et al., "NIST atomic spectra database," *National Institute of Standards and Technology, Gaithersburg, MD*, 2008.

[64] C. Kenty, "Production of 2537 radiation and the role of metastable atoms in an argon-mercury discharge," *Journal of Applied Physics*, vol. 21, no. 12, pp. 1309–1318, 1950.

[65] D. Crandall, R. Phaneuf, and G. H. Dunn, "Electron impact excitation of Hg^+," *Physical Review A*, vol. 11, no. 4, p. 1223, 1975.

[66] H. Hyman, "Electron-impact ionization cross sections for excited states of the rare gases (Ne, Ar, Kr, Xe), cadmium, and mercury," *Physical Review A*, vol. 20, no. 3, p. 855, 1979.

[67] G. Gousset, B. Sayer, and J. Berlande, "Electron-Cs^+-ion recombination in the presence of neutral helium atoms," *Physical Review A*, vol. 16, no. 3, p. 1070, 1977.

[68] V. E. Jog and M. Biondi, "Dissociative recombination of Hg_2^+ ions and electrons: dependence of the total rate coefficient and excited state production on electron temperature," *Journal of Physics B: Atomic and Molecular Physics*, vol. 14, no. 23, p. 4719, 1981.

[69] M. A. Biondi, "Processes involving ions and metastable atoms in mercury afterglows," *Physical Review*, vol. 90, no. 5, p. 730, 1953.

[70] J. S. Cohen, R. L. Martin, and L. A. Collins, "Chemi-ionization of mercury atoms: Potential curves and estimates of the total ionization cross sections," *Physical Review A*, vol. 66, no. 1, p. 012717, 2002.

[71] S. Majetich, E. M. Boczar, and J. R. Wiesenfeld, "Energy pooling and associative ionization following laser excitation of mercury vapor," *Journal of Applied Physics*, vol. 66, no. 2, pp. 475–481, 1989.

[72] J. Pouvesle, J. Stevefelt, F. Lee, H. Jahani, V. Gylys, and C. Collins, "Reactivity of metastable helium molecules in atmospheric pressure afterglows," *The Journal of Chemical Physics*, vol. 83, no. 6, pp. 2836–2839, 1985.

[73] A. K. Belyaev, "Charge exchange with ion excitation in collisions of helium ions with mercury atoms," *Journal of Physics B: Atomic, Molecular and Optical Physics*, vol. 26, no. 21, p. 3877, 1993.

[74] H. Kano, T. Shay, and G. Collins, "A second look at the excitation mechanism of the He-Hg^+ laser," *Applied Physics Letters*, vol. 27, no. 11, pp. 610–612, 1975.